Alma Mater Studiorum – Università di Bologna

DOTTORATO DI RICERCA IN

Scienze Biomediche e Neuromotorie

Ciclo XXXIV

Settore Concorsuale: 05/D1

Settore Scientifico Disciplinare: BIO/09

Neural states in parietal areas during arm reaching

Presentata da: Stefano Diomedi

Coordinatore Dottorato

Prof.ssa Matilde Yung Follo

Supervisore

Prof.ssa Patrizia Fattori

Esame finale anno 2021

Index

1 Abstract

Since the first subdivisions of the brain into macro regions, it has always been thought a priori that, given the heterogeneity of neurons, different areas host specific functions and process unique information in order to generate a behaviour. Moreover, the various sensory inputs coming from different sources (eye, skin, proprioception) flow from one macro area to another, being constantly computed and updated. Therefore, especially for non-contiguous cortical areas, it is not expected to find the same information. From this point of view, it would be inconceivable that the motor and the parietal cortices, diversified by the information encoded and by the anatomical position in the brain, could show very similar neural dynamics. With the present thesis, by analyzing the population activity of parietal areas V6A and PEc with machine learning methods, we argue that a simplified view of the brain organization do not reflect the actual neural processes.

We reliably detected a number of neural states that were tightly linked to distinct periods of the task sequence, i.e. the planning and execution of movement and the holding of target as already observed in motor cortices. The states before and after the movement could be further segmented into two states related to different stages of movement planning and arm posture processing. Rather unexpectedly, we found that activity during the movement could be parsed into two states of equal duration temporally linked to the acceleration and deceleration phases of the arm. Our findings suggest that, at least during arm reaching in 3D space, the posterior parietal cortex (PPC) shows low-level population neural dynamics remarkably similar to those found in the motor cortices. In addition, the present findings suggest that computational processes in PPC could be better understood if studied using a dynamical system approach rather than studying a mosaic of single units.

2 Introduction

The “cognitive functions”, as perception to action, are the foundation of our interaction with the world. These are tools that permitted us to perform a wide variety of complex tasks and they are supported by the cooperation of different brain regions at the same time, from the more sensory to the more motor and associative ones each with a particular function. The cerebral processes generating motor output, such as movements to reach and grasp objects, encompass several neural computations during the planning, preparation, execution and the online control of an action. These computations are carried out by associative cortices, for example the somatomotor and visuomotor areas of the superior parietal lobe (SPL, Gamberini et al., 2020; Passarelli et al., 2021) that occupies the medial part of the posterior parietal cortex (PPC). In fact, each of these areas are connected with a set of visual, somatosensory, motor and premotor areas (Bakola et al., 2010, 2013, 2017; Gamberini et al., 2009; Passarelli et al., 2011, 2018). Thus, SPL receives information from multiple sensory sources that are integrated with motor input sent by areas of the frontal cortex, in order to generate a complex motor response (Hyvärinen et al., 1982; Mountcastle et al., 1975). In particular SPL areas are involved during arm reaching movements (Fattori et al., 2001, 2005; Ferraina et al., 1997; Hadjidimitrakis et al., 2015; Hwang et al., 2014; McGuire and Sabes, 2011).

SPL receives both visual and somatosensory inputs and here, two opposite flows of information have been observed: visual information goes from the posterior to the anterior areas, whereas somatosensory information goes from the anterior to the posterior ones. Furthermore, SPL areas, especially V6A area (Fattori et al., 2005), receive copies of efferent signals from motor cortices, such as F2 and F7 (Gamberini et al., 2009; Matelli et al., 1998; Passarelli et al., 2011; Shipp et al., 1998). All these signals are integrated and then sent to by motor cortices to monitor actions (Fattori et al., 2017).

Despite this simple and schematic view, supported by anatomical connectivity, of how information flows through brain regions to generate movement, there is no clear understanding of their functional role. Although there are numerous studies on the frontal motor areas, no agreement regarding the basic properties of the motor cortex has been reached (Churchland et al., 2010; Churchland and Shenoy, 2007; Fetz, 1992; Graziano, 2008, 2011; Hatsopoulos, 2005; Mussa-Ivaldi, 1988; Reimer and Hatsopoulos, 2009; Scott, 2000, 2008; Scott and Kalaska, 1995; Todorov, 2000). On the contrary, technological developments in electrophysiological techniques and the possibility of exploiting higher computational resources have led to the cohesion of several theories (Omrani et al., 2017). Turning to the association areas, like SPL, the situation is even worse. The lack of studies with modern approaches and the intrinsic heterogeneity of its neurons do not allow us to understand how it interacts with frontal motor areas to guide movement and, accordingly how it could be framed within the theory

of motor control. The objective of this thesis will be to study two areas of the SPL, V6A and PEc, with modern computational approaches, in order to contextualise them within the fronto-parietal network and so highlighting their neural basis during movement preparation, generation and control.

2.1 Single cell *vs.* Population approach

The classical scientific approach used by neurophysiologists was to record, using single electrodes, the activity of individual neurons in behaving animals with the aim of understanding how motor behaviour is produced. Animals are trained to perform behavioural tasks, designed to test a particular hypothesis. After the recording session the researcher selects task-related cells to understand which motor parameters each cell encodes. This is called 'single cell' approach and it is usually used to relate neural activity to task parameters. However, this approach introduces bias: the recorded activity can be only interpreted in relation to the task, and the task was defined precisely to test the researcher's hypothesis ('taks-induced bias') and only neurons explicitly task related were considered for analysis ('selection bias') (Fetz et al., 1992). In addition, this approach does not take into account the interactions between neurons and it leads to the inevitable division of a neural population into clearly segregated sub-groups, each encoding a different parameter. This is in contrast with recent evidences suggesting that this clean separation is not always possible (Finkelstein et al., 2018; Fusi et al., 2016; Rentzeperis et al., 2014; Rigotti et al., 2013; Walker et al., 2011).

Nowadays, hundreds of neurons can be recorded simultaneously, thanks to technological development and the possibility to store and analyze big amounts of data. The introduction of the population approach was necessary to study these more informative neural data set (in which interaction can be taken into account) and to remove the analytical bias. Moreover, if single cell approaches can help to investigate *how* neural computations are carried out, we need to consider the entire population of neurons (or at least the recorded ones) to get insights on *what* the brain is computing (Churchland et al., 2012; Fetz 1992; Gallego et al., 2017, 2018; Shenoy et al., 2013). Despite the almost infinite activity patterns that theoretically could be observed, the connectivity of the underlying network constrains the population to activate according to a few possible activation patterns, which are called 'neural modes', especially in typical laboratory tasks (Gallego et al., 2017, 2018; Gao and Ganguli, 2015). Rather than the contributions of single cells, it is the activation of these neural modes that shapes the ensemble activity (Gallego et al., 2017, Luczak et al., 2015; Sadtler et al., 2014; Shenoy et al., 2013). Such a dimensionality reduction implies a high redundancy in neural discharges and furthermore the contribution of each unit to more than one population 'neural mode'. In fact, there is not the necessity to record every single neuron in an area to decode information, but it is possible to use only a small fraction of neurons (Gao and Ganguli, 2015).

2.2 New insights on Motor Cortex

The frontal cortex it is the region of the brain more involved in the planning, control and execution of voluntary movement. It is directly linked to spinal cord by motor neurons and contains a topographic map of motor output to different parts of the body (Beevor and Horsley, 1890; Grunbaum and Sherrington, 1903). It could be divided into two main functional areas (Campbell, 1905; Fulton, 1934, 1935; Vogt and Vogt, 1919): the primary motor cortex (M1) that is located in the pre-central gyrus in front of the central sulcus, and the premotor cortex (PM) located anteriorly to M1.

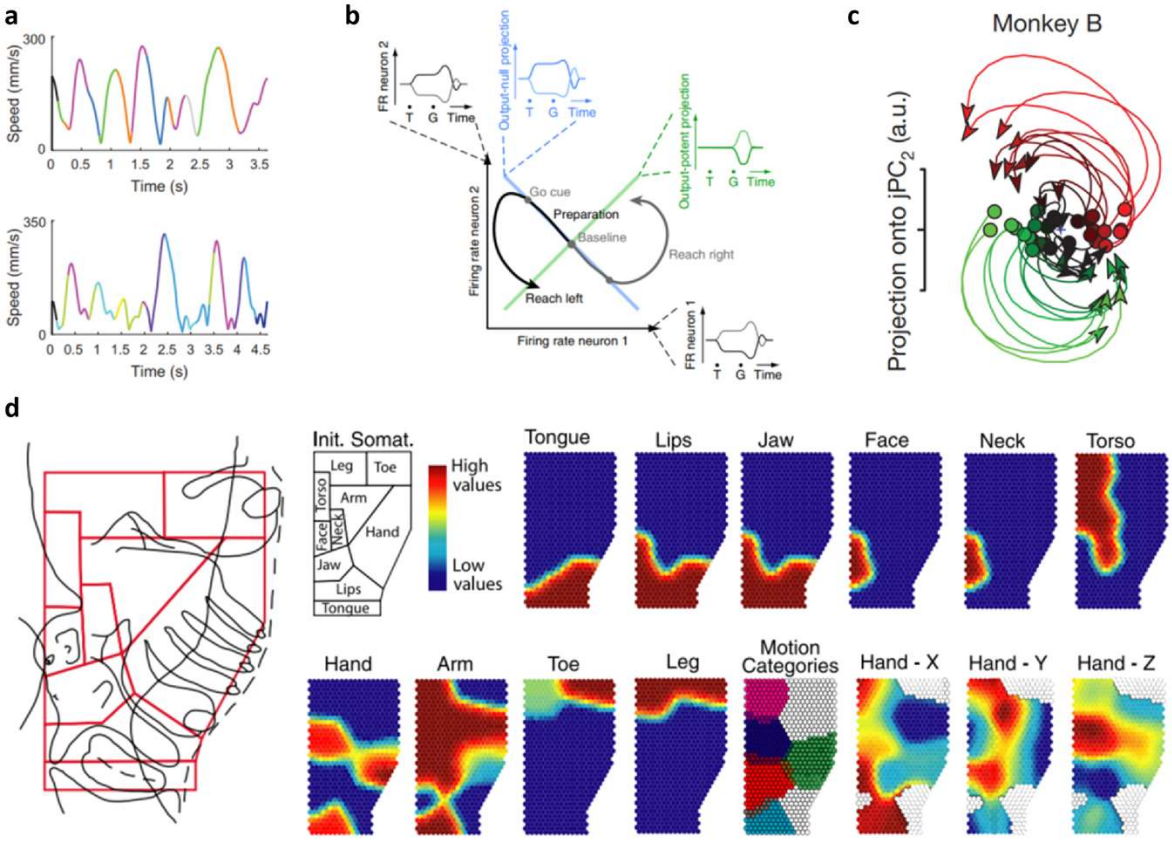

Figure 1. New theories regarding motor processing. A) Hand velocity profile during random target pursuit task in two exemplar trials. Color code represents the different states of acceleration and deceleration computed using Hidden Markov Model. Modified from Kadmon Harpaz et al., 2019. B) Schematic representation of output-null model. Whether neural activity changes within the output-null space (represented in blue) muscles keep their activity constant and movement does not begin, whereas if activity varies in the output-potent space (represented in green), the activity of muscles changes and movement is performed. Modified from Kauffman et al., 2014. C) Neural activity projection of 74 neurons during 28 different reach conditions that shows the rotational low-dimensional dynamic. Every curve represents neural population from the preparatory states (circles) to the first 200 ms of the movement. Modified from Churchland et al., 2012. D) From left to right: black and white map represent Woolsey's map with a schematized somatotopy superimposed. Colored maps represent the result of the self-organizing map model for 10 body parts, motion categories and hand location (x,y,z). Modified from Aflalo and Graziano 2006.

The well accepted view is that the first one should be involved directly in movement execution, whereas the second one in the selection of the appropriate motor plans (Kandel et al., 2013).

Based on single cell studies, motor cortex has been reported to process either low level signals such as force exerted (Evarts, 1968), torques (Scott and Kalaska, 1997), velocity, acceleration, direction or a combination of these (Ashe and Georgopoulos, 1994) and high-level movement kinematics (Georgopoulos et al., 1982). Recent advances in understanding motor processing were made by studies that, using modern mathematical approach, were focused on the activity of large populations of neurons. In such a work, Kadmon Harpatz and collegues (2019) showed that the role of M1 is to control the different elementary phases of acceleration/deceleration that can be combined to generate several complex motor responses (Figure 1a). The dynamical system approach' where neural activity is modelled as a system whose future state depends only from the previous one, its input and noise, revealed that neural patterns generated by motor cortex can be subdivided in 'output-potent', directly related to muscle control, and 'output-null' representing internal computation (Figure 1b; Kaufmann et al., 2014). Moreover, by exploiting dimensionality reduction techniques, it is possible to represent population activity as a curve, called neural trajectories, embedded in a 3D space, called state-space where each axis captures one or more neuron's response, or a factor shared by neurons. In the motor and premotor state-space, rhythmic and rotational neural trajectories have been identified; they indicate low-dimensional dynamic, with the functional role to produce oscillatory temporal patterns needed to generate multiphasic muscle activity (Figure 1c; Churchland et al., 2012, Shenoy et al., 2013). Classic knowledge about the topographical organization of the motor cortex as a rough map of the body's musculature, explained by the *homunculus*, has been revised by Graziano and Aflalo that, using a neural network, proved that motor cortex can be organized on the basis of several categories of action involving the cooperation of several body parts (Figure 1d; Aflalo and Graziano, 2006; Graziano and Aflalo, 2007).

2.3 Hidden Markov Model

Nowadays the literature is rich of several mathematical methods used to investigate neural population activity in their different aspects: classic dimensionality reduction methods like Principal Component Analysis that is able to explain a fixed percentage of variance inside the population (Cunningham and Yu, 2014), Tensor Decomposition Analysis can be used to reveal learning dynamics (Williams et al., 2018) or Graph Theory used to discover functional hierarchical topological organization (Bardella et al., 2020).

In recent years, the use of machine learning approaches has become increasingly widespread not only in the neuroscience field (Shinde and Shah, 2018). These techniques allow computers to solve specific tasks without having been explicitly programmed by humans to solve them and thus reducing human bias. This is done through self-learning techniques that allow computers to learn from the data

provided, usually called a "training set". Once trained, the computer can solve specific task from unseen data, usually called a "validation set". Among the unsupervised machine learning approaches, the Hidden Markov Models (HMMs) are widely used to analyse time series data. This method has been exploited in speech recognition (Rabiner, 1989), visual recognition (Bicego et al., 2005) and in the recognition of biological sequences, in particular amino acids in proteins and nitrogen bases within DNA (Yoon, 2009). In the neuroscience field, the idea behind the HMM analysis is that neural activity passes through a series of discrete states that are not directly observable. Starting from a recording of a neural ensemble, HMMs give us the possibility to detect different patterns of activity, defined 'neural hidden states' in the context of Markovian processes and that resemble some aspects of the 'neural modes' (Gallego et al., 2017, 2018; Gao and Ganguli, 2015). In other words, starting from discrete neural recordings in a certain time interval, HMM can be used to classify neural patterns in each discrete time. Abeles and co-workers proved that the frontal areas, during an arm movement, passed through a sequence of distinct neural states in which the firing rate of the considered neural population were approximately stationary and depending by the cooperative action of many neurons (Abeles et al., 1995).

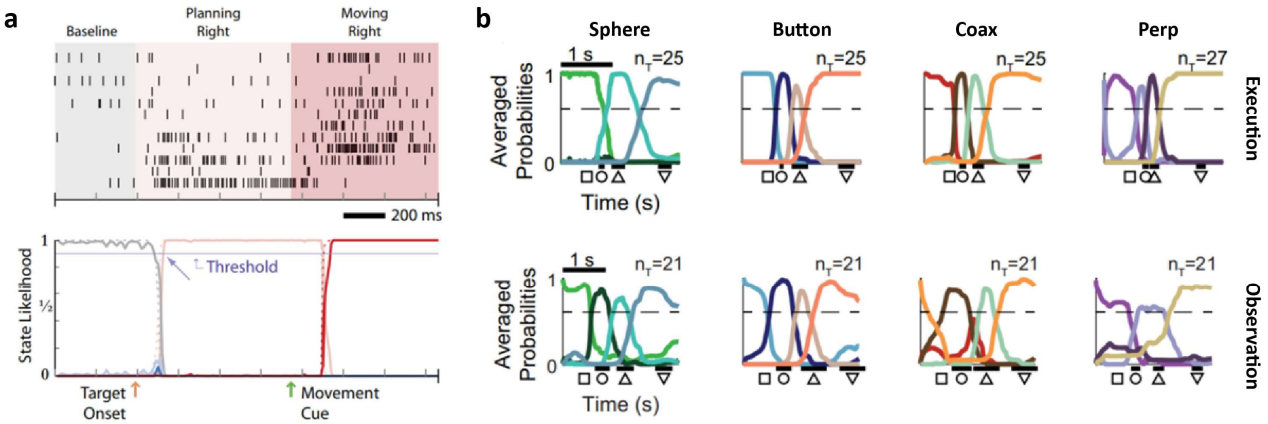

Figure 2. HMM application in premotor and motor cortex. A) Top: example raster of neural activity during rightward movement. Bottom: Decoded neural states of an individual trial. Colored line represents the time course of the probability of each state. Horizontal line: threshold set to identify 'active' states. Modified from Kemere et al., 2008 B) Top: Average decoded probability neural states across Execution trials for each object using premotor mirror neurons. Bottom: Average decoded probability neural states across Observation trials for each object using premotor mirror neurons. Modified from Mazurek et al., 2018.

In primary motor cortex it was demonstrated that the time of transition from a baseline activity to the planning of a reaching, that has no immediate observable behavioural response, can be detected with HMM (Figure 2a, Kemere et al., 2008). Moreover, Kadmon Harpaz et al. (2019) found different neural states corresponding to acceleration and deceleration phases with directional selectivity. In M1and pre-motor cortex, HMMs was used to compare two different neural subpopulations showing

that both mirror and non-mirror neurons represented the entire behavioural sequence of an arm reaching movement (Figure 2b, Mazurek et al., 2018). In addition to the functional properties that can be deduced from these 'neural states', HMMs can be used as neurodecoder to control brain machine interfaces (BMIs, Kang et al., 2015, Kao et al., 2017; Kemere et al., 2008; Shenoy et al., 2003).

To our knowledge, no attempt to apply HMM has been done for what concerns motor tasks, even if parietal cortices are known to play a central role in sensory and motor processing (Cisek and Kalaska, 2010; Hadjidimitrakis et al., 2017, 2019; Medendorp and Heed, 2019; Passarelli et al., 2021; Pezzulo and Cisek, 2016). For this reason, in the present thesis, we applied HMMs analysis on neural activity recorded from parietal areas V6A and PEc located in the superior parietal lobule of macaque brain.

2.4 Posterior Parietal Cortex

The posterior parietal cortex (PPC) is shaped by anatomically and functionally different areas and it is classically defined an 'association cortex' due to the different sensory signals that are integrated. Its connections with sensory and motor areas, and the discovery of somatomotor, visuomotor, oculomotor and attentional activities (Andersen et al., 1997; Bakola et al., 2010, 2013; Caminiti et al., 2015; Fattori et al., 2005; Filimon, 2010; Galletti et al., 2003, 2010; Gamberini et al., 2009, 2021; Gottlieb, 2007; Kalaska, 1996; Passarelli et al., 2011, 2021; Pisella et al., 2017; Sereno and Huang, 2014) supports the role of computing visuo-motor transformations needed in the guidance of arm reaching (for grasping) movements.

Accordingly, in the ''Two Visual Systems Hypothesis'' (Ungerleider and Mishkin, 1982), PPC belonged to the 'dorsal visual stream' that is involved in the visual guidance of prehension. A more recent view of this hypothesis (Galletti et al., 2003; Rizzolati and Matelli, 2003) subdivided this stream into two sub-streams, a more medial one, called 'dorso-medial visual stream' running from the visual areas through the superior parietal lobule (SPL) to the frontal cortex, and the 'dorso-lateral visual stream' that involves the inferior parietal lobule (IPL) areas instead of SPL (Figure 3). The first one uses visual information to constantly monitor the spatial position of an object, in foveated or peripherical condition, in order to allow optimal reaching and grasping action especially in dynamic contexts (Fattori et al., 2017; Galletti et al., 2004; Galletti and Fattori, 2018). The second one exploits visual information to recognize the characteristic of an object to be grasped like shape, dimension and orientation (Galletti et al., 2001; Galletti and Fattori, 2003; Galletti and Fattori, 2018; Pitzalis et al., 2013; Tootell et al., 1995).

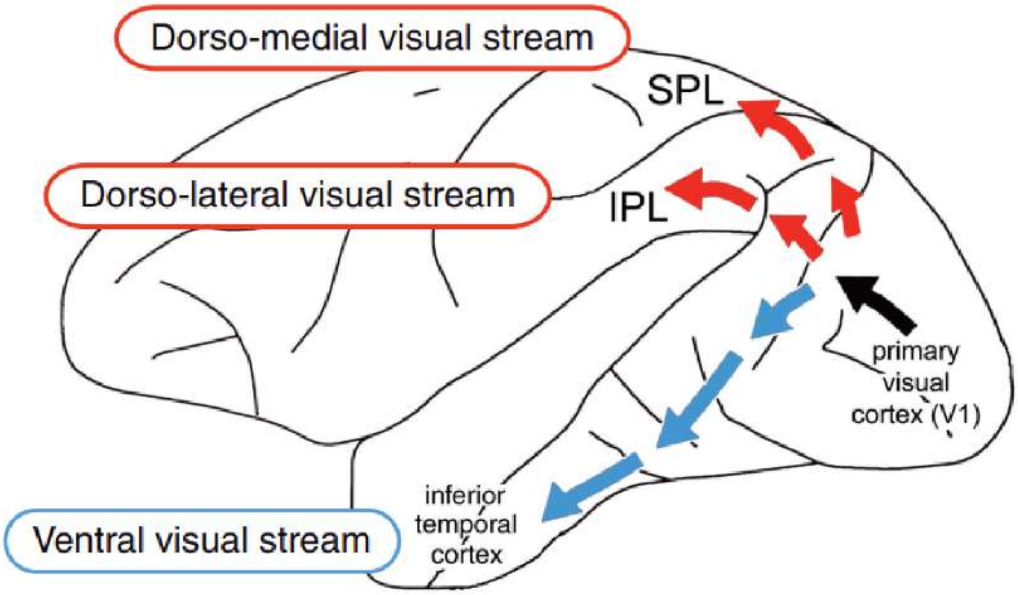

Figure 3. Visual streams in macaque brain. Lateral views of the macaque brain. Blue arrows show the ventral visual stream path. In red the two subdivisions of the dorsal visual stream, the dorso-lateral visual stream towards the inferior parietal lobule and the dorso-medial visual stream towards the superior parietal lobule. Modified from Fattori et al., 2017.

2.5 V6A and PEc Areas

In the context of 'dorso-medial visual stream' our analysis includes two visuo-motor areas of the SPL named V6A and PEc (Figure 6a).

On one hand, PEc corresponds to the caudal part of area PE located on the dorsal surface of SPL (Breveglieri et al., 2006, 2008; Gamberini et al., 2020; Luppino et al., 2005; Pandya and Seltzer, 1982). It has been demonstrated that PEc cells are visually responsive to moving light bars and optic flow stimuli (Figure 4a; Battaglia-Mayer et al., 2001; Ferraina et al., 2001; Squatrito et al., 2001), but they are also modulated by passive somatosensory inputs, such as arm joint rotations (Figure 4b; Breveglieri et al., 2006, 2008; Gamberini et al., 2018), by arm reaching (Figure 4c; Batista et al., 1999; Battaglia-Mayer et al., 2001; Ferraina et al., 2001; Hadjidimitrakis et al., 2015) and by eye movements (Figure 4d; Battaglia-Mayer et al., 2001; Ferraina et al., 2001).

On the other hand, V6A is located posteriorly, in the dorsal part of the anterior bank of the parieto-occipital sulcus (Galletti et al., 1996; Gamberini et al., 2020, Luppino et al., 2005). Area V6A is a visuomotor area that contains visual neurons (Figure 5a; Galletti et al., 1999; Gamberini et al., 2011) and somatic cells almost exclusively arm-related (Figure 5b; Breveglieri et al., 2002; Gamberini et al., 2011).

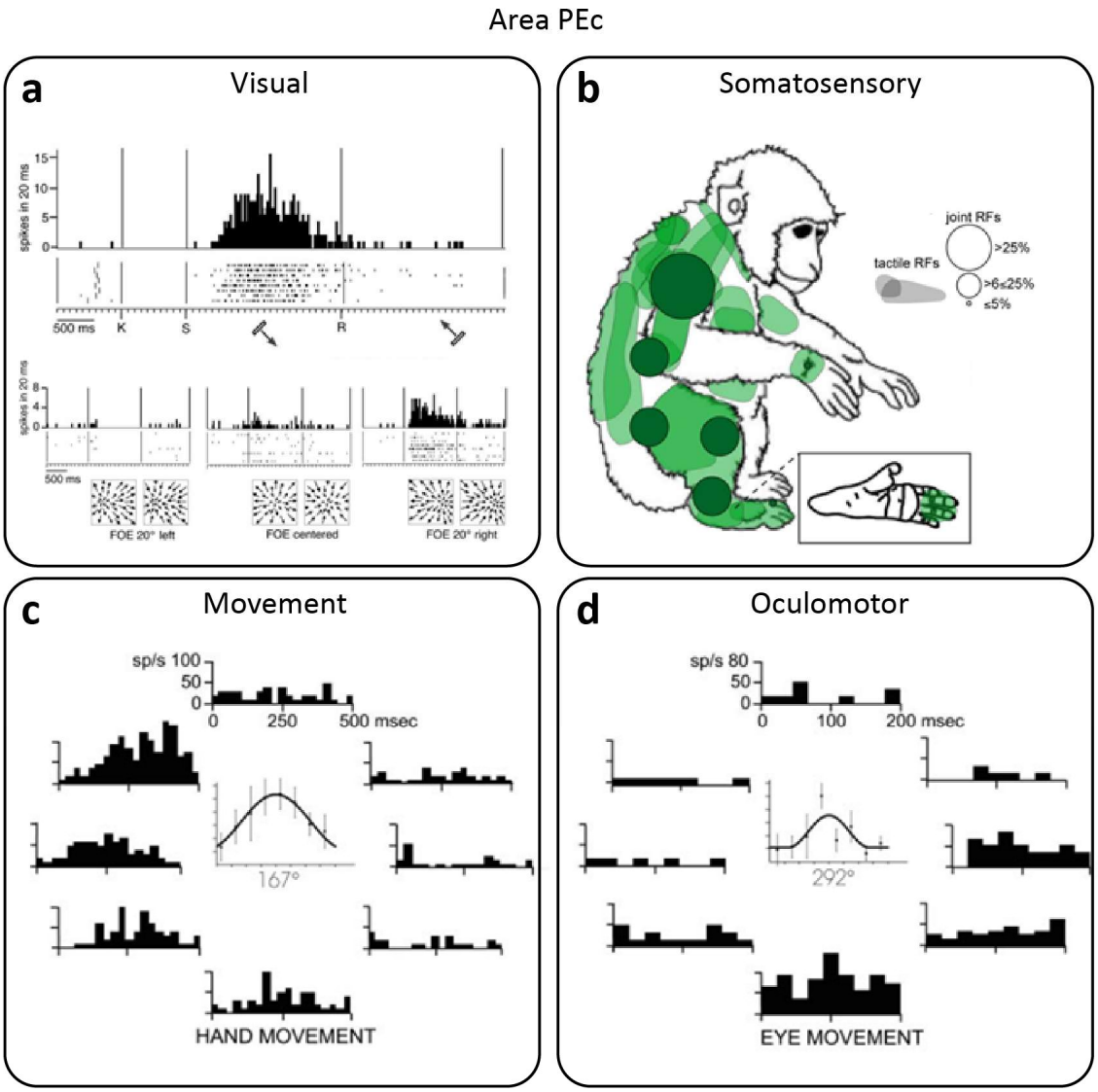

Figure 4. Functional properties of PEc neurons. A) Top: cell modulated by a light bar moving across visual field, plots represent peri-event time histogram and raster. Marker events: 'K' trial onset, 'S' stimulus appears and it starts moving in one direction, 'R' the stimulus reverses the direction of movement. Bottom: cell modulated by radial optic flow stimulation. Faring rate is modulated by particular focus of expansion (FOE) and positions respect to the fixation point. Modified from Battaglia-Mayer et al., 2001. B) Body map with somatosensory (patches) and joints (circles) receptive fields (RFs) location. Only RFs of animal's right side are reported. RFs of the body parts not visible are reported in the animal's left side. Modified from Gamberini et al., 2020 C) Peri-event time histograms (peripheral) and tuning curve (center) of cell modulated by reaching direction (Reach-Fixation task). Modified from Battaglia-Mayer et al., 2001. D) Peri-event time histograms (peripheral) and tuning curve (center) of cell modulated by eye movement direction (Saccade task). Modified from Battaglia-Mayer et al., 2001.

Arm-reaching direction and depth tune V6A discharges both during planning and execution (Figure 5c; Bosco et al., 2010; Fattori et al., 2005; Gamberini et al., 2011; Hadjidimitrakis et al., 2014, 2015; 2017, Santandrea et al., 2018). Neural correlates of oculomotor activity have been also found in this area (Figure 5d; Breveglieri et al., 2012; Galletti et al., 1995; Hadjidimitrakis et al., 2011, 2012, 2020; Kutz et al., 2003). Furthermore, while PEc seems to exhibit a slightly more somato-motor related

activity (having, for example, neurons responsive to somato-sensory stimuli from the lower limb that are absent in V6A), V6A cells are more often modulated by visual stimuli (Bakola et al., 2010; Gamberini et al., 2011, 2018; Hadjidimitrakis et al., 2015).

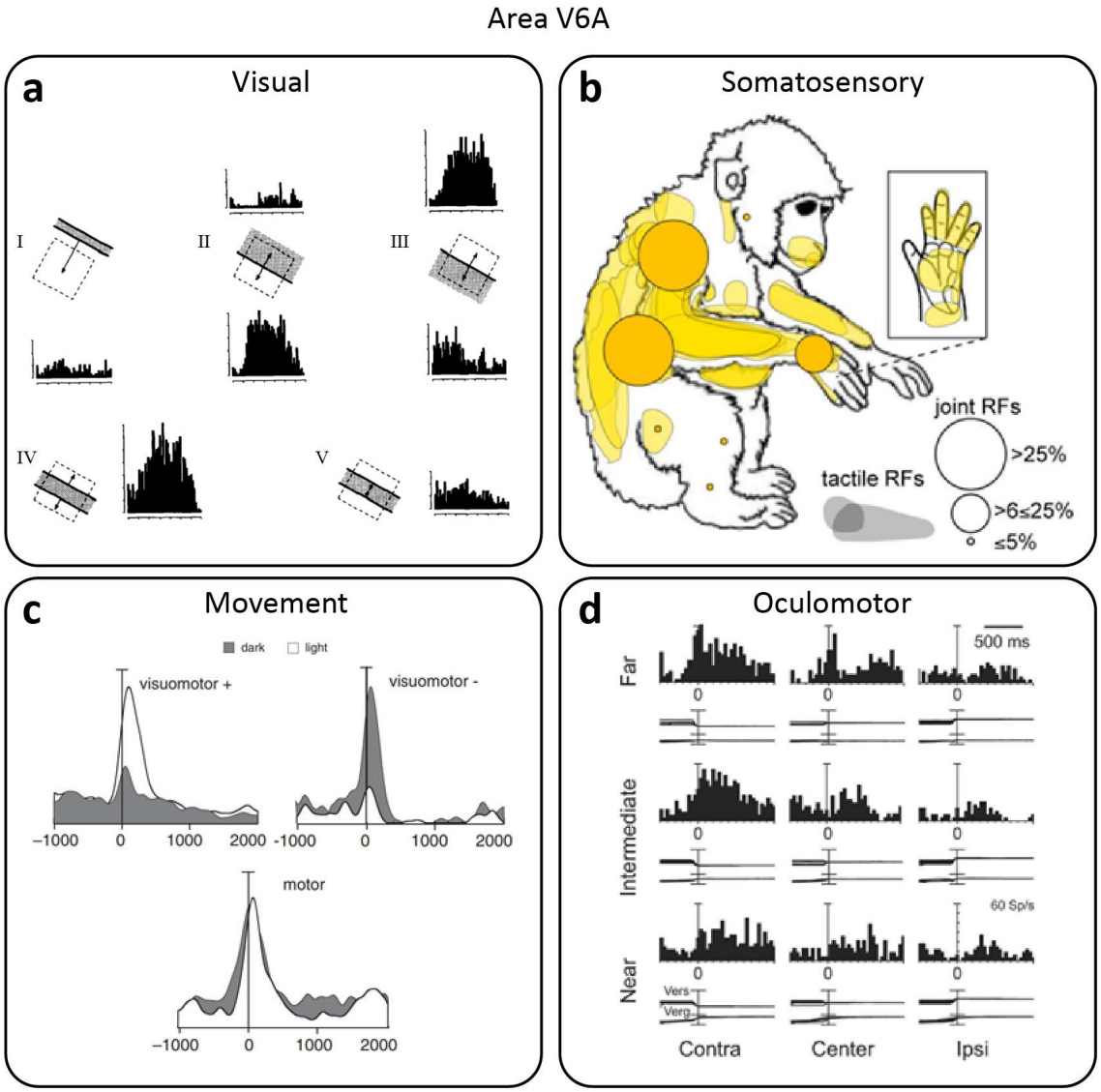

Figure 5. Functional properties of V6A neurons. A) Modulation of a neuron to moving bars (I), edges (II and III), expansion and contraction of a dark bar (IV and V). Modified from Galletti et al., 1996. B) Body map with somatosensory (patches) and joints (circles) receptive fields (RFs) location. Only RFs of animal's right side are reported. RFs of the body parts not visible are reported in the animal's left side. Modified from Gamberini et al., 2020. C) Three types of neurons modulated by reaching activity in dark (gray) and light (white) condition: 'visuomotor+' neuron modulated only in light, 'visuomotor-' neuron modulated only in dark, 'motor' neuron modulated independently by visual feedback. Neural activity is aligned to the onset of the movement (0). Modified from Fattori et al., 2017. D) Example of neuron modulated by version. Plots are arranged according to the spatial position of 9 targets (3 different depth level for 3 different direction). Data is aligned to 'saccade onset'. Modified from Breveglieri et al., 2012.

About anatomical connectivity, PEc is strongly connected with F2 and has weak connections with F1, it also receives afferents from many parietal areas (PE, MIP, PG, PGop, PEci) including V6A (Figure 6b; Bakola et al., 2010). Instead, V6A is connected with frontal cortex areas F2 and F7

(Gamberini et al., 2009; Passarelli et al., 2011), moreover it receives visual information, from occipital lobe areas (V2, V3, V4, MST, V6) and parietal visuomotor areas like AIP and LIP, and somatosensory and somatomotor inputs from PEc and MIP (Figure 6c; Bakola et al., 2010, 2017).

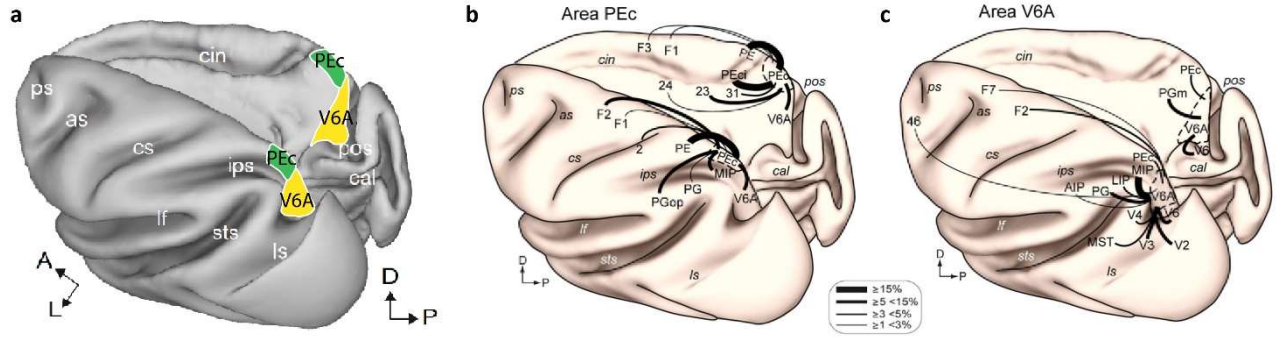

Figure 6. Anatomical location and connections of Area PEc and V6A. A) Three-dimensional reconstruction of macaque brain. Dorsal view of the left hemisphere and medial view of the right hemisphere showing area PEc in green and V6A in yellow. Modified from Diomedi et al., 2021. B-C) Summary of the cortico-cortical connections of areas PEc and V6A. Thickness of lines are proportional to the strength of connections. Connections are averaged across cases with injections in the same area. Modified from Gamberini et al., 2020. ps, principal sulcus; as, arcuate sulcus; cin, cingulate sulcus; cal, calcarine sulcus; cs, central sulcus; ips, intraparietal sulcus; ls, lunate sulcus; pos, parieto-occipital sulcus; sts, superior temporal sulcus; D, dorsal; P, posterior; A, anterior; L. lateral.

So both areas, V6A and PEc, are connected to F2, in particular: PEc with the part of F2 that encodes more the lower limbs than the upper limbs while, on the contrary, V6A riceves inputs from the part of F2 that represents more the upper limbs. The rest of the connections are functionally different: PEc in more connected with somatic cortical areas while V6A with the visual one.

So, despite distinct anatomical differences, concerning cyto/myeloarchitecture (Luppino et al., 2005) and anatomical connections (Bakola et al., 2010; Gamberini et al., 2009), the two areas shows similarities of visual and somatosensory properties (Gamberini et al., 2018) and motor-related activity (Battaglia-Mayer et al., 2001; Fattori et al., 2005; Ferraina et al., 2001; Hadjidimitrakis et al., 2014, 2015; Piserchia et al., 2017) with a prevalence of somatosensory properties in PEc and visual ones in V6A.

2.6 Aim of the thesis

Applying the HMM technique to neural data of two animals recorded during a fix to reach task toward 9 targets located at three different directions and depths in the peripersonal space, we address multiple open questions:

1) Can the variety of single unit discharges be traced back to a finite, low number of population patterns?

2) If yes, to which neural process are they related and what is the temporal evolution of these neural patterns?

We argue that the latter question can be solved by following two different hypotheses:

(1) neural states are stable across different trials and they are time locked to the animal behaviour

(2) neural states are not stable, especially across different targets, and so they have a high variable timing of transition.

Furthermore, once one of the two hypotheses is confirmed, we are going to understand whether these neural states are supported by the entire population or whether each state is generated by a clearly separated sub-groups of neurons.

3 Materials and Methods

The current study consisted in an extended computational analysis of neural data reported previously (Hadjidimitrakis et al., 2014, 2015). Accordingly, the procedures described herein focus on analytical treatment of the data and provide only essential details of the experimental procedures. Full details of experimental methods are provided in published papers (Breveglieri et al., 2014, 2015; Galletti et al., 1995).

The study was performed in accordance with the guidelines of the EU Directives (86/609/EEC; 2010/63/EU) and the Italian national law (D.L. 116-92, D.L. 26-2014) on the use of animals in scientific research. Protocols were approved by the Animal-Welfare Body of the University of Bologna. During training and recording sessions, particular attention was paid to any behavioural and clinical sign of pain or distress.

3.1 Experimental Procedures

Two male macaque monkeys (Macaca fascicularis) weighting 4.4 kg (M1) and 3.8 kg (M2) were used. Single cell activity was extracellularly recorded from the anterior bank of the parieto-occipital sulcus (POs) and the adjacent caudal part of SPL.

Multiple electrode penetrations were performed using a five-channel multielectrode recording system (Thomas Recording GmbH, Giessen, Germany). The electrode signals were amplified (at a gain of 10,000) and filtered (bandpass between 0.5 and 5 kHz). Action potentials in each channel were isolated with a waveform discriminator (Multi Spike Detector; Alpha Omega Engineering Nazareth, Israel) and were sampled at 100 kHz. The quality of single-unit isolation was determined by the visual inspection of spike wave forms and considering refractory periods in ISI histograms during spike-sorting. Only well-isolated units with homogenous waveforms and clear ISI histogram were considered. The animal behaviour was controlled by custom-made software implemented in Labview (National Instruments, Austin, TX) environment (Kutz et al., 2005). Eye position signals were sampled with two cameras (one for each eye) of an infrared oculometer system (ISCAN, Woburn, MA) at 100 Hz. The vergence angle was not recorded online, but it was reconstructed offline from the horizontal eye positions of the two eyes. A sort of control for vergence resulted from the presence of electronic windows (one for each eye, 4° × 4° each) that controlled the frontoparallel gaze position, so that we could set an offset of the horizontal eye position signal for targets located in the same direction, but at different depths.

Histological reconstruction of electrode penetrations was performed following the procedures detailed in studies from our lab (Gamberini et al., 2011, 2018). Briefly, electrode tracks and location of each recording site were reconstructed on Nissl-stained sections of the brain on the basis of several

cues: 1) marking electrolytic lesions, 2) the coordinates of penetrations within the recording chamber, 3) whether the electrode passed through another cortical area before reaching the region of interest. Area V6A was initially recognized on functional grounds following the criteria described in Galletti et al. (1999) and later confirmed based on the cytoarchitectonic criteria reported in Luppino et al. (2005). The recording sites were assigned to area PEc according to the cytoarchitectonic criteria of Pandya and Seltzer (1982) and Luppino et al. (2005).

3.2 Behavioural Task

Electrophysiological signals were collected while the monkeys performed an instructed-delay foveated reaching task (Figure 7c), towards targets that were located at different positions in the 3D space. Monkeys sat in a primate chair, with the head restrained, and faced a horizontal panel located at eye level. Nine light-emitting diodes (LEDs) mounted on the panel at different directions and distances from the eyes were used as both fixation and reaching targets (Figure 7b, left). As shown in the right part of Figure 7b, the LEDs were arranged in three rows: one central, along the sagittal midline, and two laterals, at version angles of −15° and +15°, respectively. Along each row, three LEDs were located at vergence angles equal to 17.1°, 11.4°, and 6.9°, respectively. The two animals had the same interocular distance (3.0 cm), so the targets in each row were placed at the same distance from the monkeys' mid-eye level in both animals (nearest/intermediate/far targets: 10/15/25cm, respectively). The range of vergence angles was chosen to be within the limits of peripersonal space, so the monkeys were able to reach all target positions. The animals performed the task with the limb contralateral to the recording site while maintaining steady fixation. The hand started the trial pushing a button (home button, HB, 2.5 cm in diameter, Figure 7b) placed outside the monkeys' visual field, 5 cm in front of its trunk. After 1 sec, one of the nine LEDs lit up green and the monkeys were required to fixate it while keeping the button pressed. The monkeys had to withhold any eye or arm movement for 1700–2500 ms, until the 'go' signal that was the change of LED colour (green to red). After the 'go' signal the animal had 1 sec to release the HB (movement onset) and start an arm movement to reach the target. Target touch was acquired as the activation of a micro-switch positioned at LED basis (movement end). After reaching the target LED the monkeys had to hold it for 800–1200 msec. Then, the LED offset cued the monkeys to release it and move their arm backward to press the HB in order to receive reward. Only rewarded trials were used in further analyses.

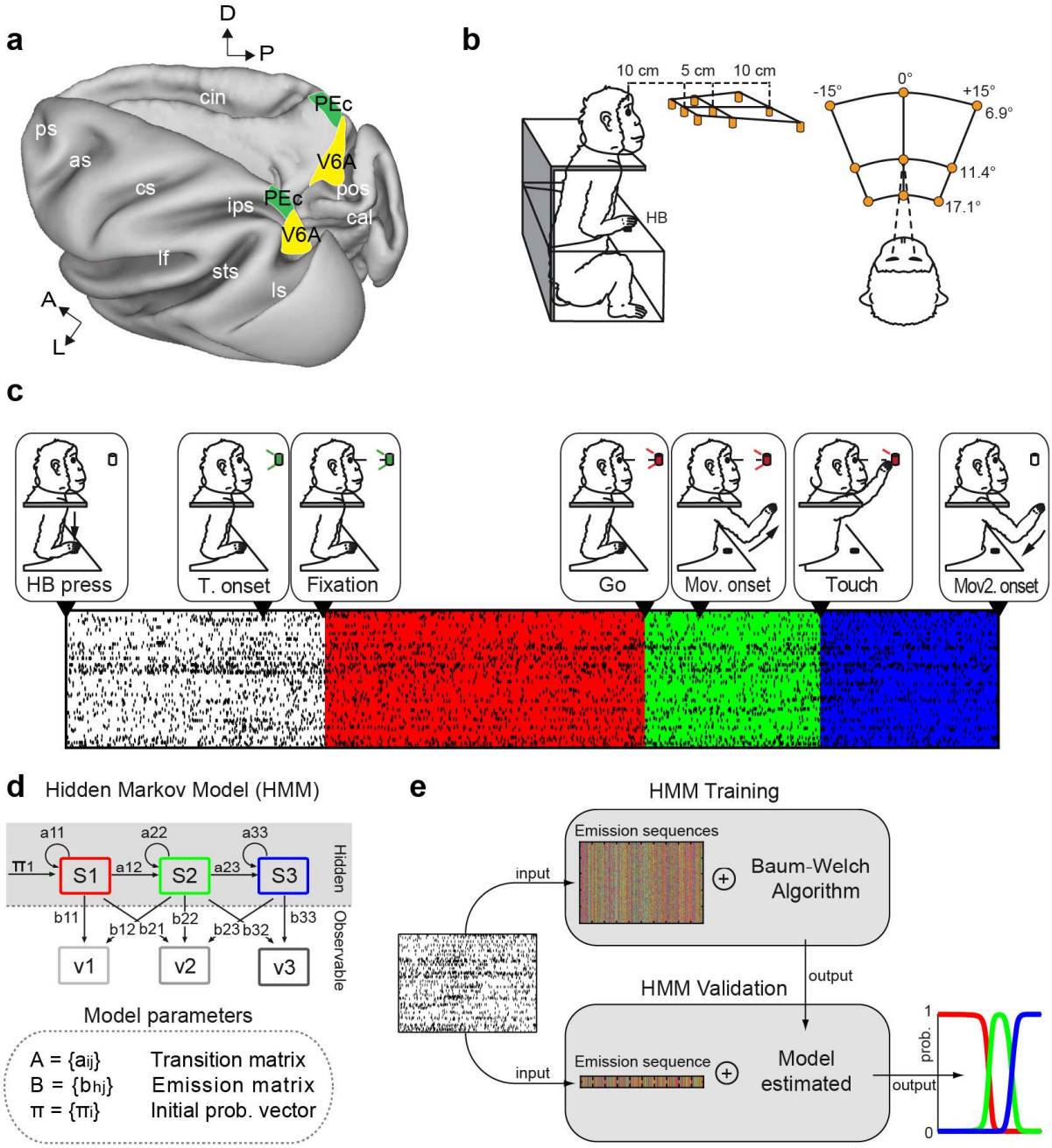

Figure 7. Anatomical localization of V6A and PEc, experimental design and Hidden Markov model. a) 3D reconstruction of macaque brain. Dorsal view of the left hemisphere and medial view of the right hemisphere showing area V6A (yellow) and PEc (green). Abbreviations: as, arcuate sulcus; cal, calcarine sulcus; cs, central sulcus; cin, cingulate sulcus; ips, intraparietal sulcus; lf, lateral fissure; ls, lunate sulcus; pos, parieto-occipital sulcus; ps, principal sulcus; sts, superior temporal sulcus; D, dorsal; P, posterior; A, anterior; L, lateral. b) Experimental setup. Reach movements were performed in darkness toward 1 of 9 LEDs arranged at eye level in front of the monkey. Spatial coordinates of targets are indicated as vergence and version angles of the eyes. HB: Home Button. c) Task sequence. From left to right: trial start (HB press), target appearance (T. onset), fixation onset (Fixation), go signal (Go), start of the arm movement (Mov. onset), touch and holding of the target (Touch), return movement (Mov2. onset). The rasters reported below are an example of neural activity pooled together to simulate an ensemble. d) Schematic representation of the HMM and its core parameters. The Markov process starts with initial probabilities π to be in one of the N states (maximum probability is assigned to the first state) and it proceeds though a series of state transitions with a probability determined by the Transition Matrix (A). The

Markov process itself is not observable (hidden), but the Emission Matrix (B) links in terms of probability this process to a series of observable events [v1, v2, v3 …] that indicate in which hidden state is the system. e) HMM training and validation on neural data. Spike counts are converted in emission sequences. During the training phase, the Baum-Welch algorithm estimates the model parameters (transition and emission matrices). These are validated on new emission sequences to give a state probability sequence (HMM validation, see Methods). From Diomedi et al. 2021.

3.3 Hidden Markov Model

We used the Hidden Markov Model (HMM) method to examine whether the PPC activity can be characterized by sequences of discrete and stable patterns of activity that are termed hidden states. The HMM assumption is that a sequence of observable symbols is generated by a sequence of underlying hidden, not directly observable states (Figure 7d). The hidden state sequence is a Markov chain (or process) since the future state of the system stochastically depends only on the present state and not on the past.

In general, an HMM is characterized by different parameters:

1. the number (N) of hidden states in the model. We called $S = \{S_1, S_2, \dots, S_N\}$ the individual state and q_t the Markov process that tell us the state at time t. The Markov process assumes the probability of transition from state S_i to S_j at time t + 1 depends only on the state of the system at time t:
$$P(q_{t+1} = S_j | q_t = S_i, q_{t-1} = S_k, \dots) = P(q_{t+1} = S_j | q_t = S_i)$$
2. the number (M) of distinct observable symbols i.e. the alphabet size. We denote symbols as $V = \{v_1, v_2, \dots, v_M\}$. A so-called emission sequence is formed by symbols in V and it represents the experimental observations. We will use these emission sequences to train and validate the model.
3. According to the Markov Process, the probability to switch from a hidden state to another (state transition) is given by the transition matrix $A = \{a_{ij}\}$ where:
$$a_{ij} = P(q_{t+1} = S_j | q_t = S_i), \quad 1 \leq i, j \leq N$$
Noteworthy, this matrix tells which status steps are allowed and which not, so it defines the topology of the Markov Process itself. Indeed, if the system can go from any state to another, we will have $a_{ij} > 0 \quad \forall i, j$. If some changes of states are not allowed, we will have the relative element $a_{ij} = 0$.
4. The emission matrix $B = \{b_{hj}\}$ links the hidden state sequence (i.e. the Hidden Markov Process) to the observable emission sequence. In brief, it represents the probability to observe the h^{th} symbol during the j^{th} state and so:

$$b_{hj} = P(v_h \; at \; t | q_t = S_j)$$

For neural data, the emission matrix represents the probability to observe a spike from the h[th] neuron during the j[th] state.

5. The vector initial probability $\pi = \{\pi_i\}$ indicates the initial probability for each HMM state at the first observation:

$$\pi_i = P(q_1 = S_i) \quad 1 \leq i \leq N$$

The initial probability is required to initiate the Markov Process.

A Hidden Markov Model is identified by these three parameters (*A, B, π*).

3.3.1 HMM training and decoding of hidden states probability

We use the Baum-Welch algorithm to train the models and so to estimate its main parameters, i.e. the transition and the emission matrix (Figure 7e). This algorithm is an iterative procedure, based on the Expectation Maximization algorithm, that starting from an initial model defined by choosing randomly initial parameters, it iteratively generates a new model upgrading the initial parameters and maximizing the probability that the new model has generated the experimental observations used. The algorithm ends either after 500 iterations or when the difference between the log-likelihood of the model at k[th] step and that of the (k-1)[th] is less than 10^{-6}. Given a trained model and an entire experimental observation $n_{1:T}$ of length T (i.e. the total number of bins) we wanted to decode $P(q_t = S_j | n_{1:T})$, i.e. the probability at each time instant to be in one of the defined hidden states (Figure 7e). For this aim we used the Forward Backward algorithm. This method uses the forward density representing information from the beginning forward to the present t*:*

$$\alpha_t(j) \equiv P(n_{1:t}, q_t = S_j) = \left[\sum_{i=1}^{N} \alpha_{t-1}(i) a_{ij}\right] b_{n_t j}$$

and the backward density that represent the information from time T backward to the present t:

$$\beta_t(j) \equiv P(n_{t+1:T}, q_t = S_j) = \sum_{i=1}^{N} \beta_{t+1}(i) a_{ji} \, b_{n_{t+1} i}$$

to infer the a posteriori likelihood (APL) that is proportional to the probability we wanted to decode (Kemere et al., 2008):

$$P(q_t = S_j \mid n_{1:T}) \propto P(n_{1:T}, q_t = S_j) = \alpha_t(j) \, \beta_t(j).$$

3.3.2 Neural implementation of HMM

In our HMM implementation, we used a single observation variable approach for simplicity and in accordance with previous works (Bollimunta et al., 2012; Mazurek et al., 2018, 2019). We performed a random selection procedure during data pre-processing (see below) to account for multiple observations and avoid information loss. In particular, N was the number of the neural states that we expected to be encoded in the population activity. Our alphabet was composed by the numbers from 1 to the total number of neurons in the population plus 0 that represented the absence of spikes from any neuron. The resulting alphabet size M is equal to number of units in our population plus one. To feed the HMM algorithm, we needed to generate the appropriate emission sequences from the neural data. Starting from a spike count for each cell and each trial (2-ms bins) aligned all at the same event, in order to generate an emission sequence, we assigned one symbol to each bin (Bollimunta et al., 2012, Mazurek et al., 2018). For example, we assigned the symbol "2" to a bin in which we recorded a spike from the 2-nd neuron of our population. If no cell discharged at a particular bin, we put the symbol "0". If two or more neurons discharged in the same bin, we chose one of them in a random way. On average, in a trial we had 11% of the total bins with no spikes, 23% with only spike from 1 neuron and 66% with spikes from 2 or more neurons. Forcing these discharges in a unique emission sequence representative of the trial would create a bias due to the randomness of the choice and it would lead to a loss of information of about 42% (considering the number of spikes occurred simultaneously that would not be considered over the total). To avoid bias and the information loss, we 'augmented' the initial data by repeating 100 times/trial the procedure, thus obtaining 100 emission sequences/trial that were slightly different one from another (1000 seq. for each target position tested on 10 trials). This procedure, that could be seen as performing a kind of 'bootstrapping' within the population of neurons active in each bin, enabled us to obtain a number of emission sequences that fully represented the original data (99.98% of probability to observe the entire information with 100 seq./trial vs $\simeq$ 85% with 50 seq./trial; simulated data). For each neural population (M1, V6A and PEc; M2, V6A and PEc), we trained an HMM separately for each target position. Because the Baum-Welch maximization is sensitive to the initial values used, during the train step, we ran the algorithm 10 times for every position and population starting each time with different initial parameters and we selected the model with the highest log-likelihood (Mazurek et al., 2018). The elements of the emission matrix were initialized as equal to $1/M$. The diagonal elements of transition matrix (i.e. the probability to remain in a state) were initialized with values in the range $a_{i,i} \in [0.99, 0.999]$, and elements above the diagonal (i.e. the probability to proceed to the next state) were set as $a_{i,j} = (1 - a_{i,i})/(1 - N)\ \forall\ j > i$ where N is the total number of the states. We then normalized the rows of the matrix to obtain a total probability equal to 1.

To avoid over fitting, the models were cross validated in two different ways. For the preliminary consistency analysis (i.e. to choose the optimal number of states), we trained the models on emission sequences generated from all the available trials and we decoded sequences generated in the same way but with an additional bins shuffling step (i.e. the t^{th}-bin of the j^{th}-sequence was randomly substitute with t^{th}-bin of the i^{th}-sequence). This atypical cross-validation allowed to test the models on data not completely new, but not identical to the training dataset, with a great computational advance. For all the subsequent analyses, we used a leave-one-out cross-validation (models trained on 9 trials and validated on the 1 left out) and all the subsequent results here reported are referred to the validation dataset, never seen by the models.

3.3.3 Consistency and timing analysis

Given a trained N-state model ([N x N] transition matrix; [n° of neurons x N] emission matrix), we considered 'consistent' with the model every emission sequence in which the probabilities of N-states crossed a threshold. We arbitrarily chose the threshold to be equal to 0.7, a slightly higher value compared to similar works (e.g., 0.6 in Mazurek et al., 2018). For the timing analysis, we took the first bin in which a state rose above the threshold ('rise' of the state) or the last bin before it fell under the threshold ('fall' of the state) considering only sequences that were consistent with the model of interest. To compare V6A and PEc areas, we performed a series of Wilcoxon test ($p<0.05$, data from M1 and M2 pooled together) for each state rise and fall. We calculated the variability in the timing of the 'real' neural transitions adjusted for the timing variability of the behavioural events. To do so, we subtracted the variance of the reference event timing from the variance of the decoded neural transition timing.

3.3.4 Gini coefficient

The Gini coefficient (or index) was used to measure the sparsity of a matrix. We computed the Gini index of the emission matrices to investigate which fraction of the population was active during each hidden state. Thus, in our case, a highly sparse emission matrix (high Gini coefficient) indicated that in each hidden state only few neurons were likely to discharge. Vice versa, we expected a low Gini coefficient when each state involved the activation of the majority of the population (low sparsity of the emission matrix). To have reference values, we generated 3 blocks of synthetic [100 neurons x 3 states] emission matrices (10,000 each block). The first block contained matrices with only a random element between 0 and 1 for each row simulating a population of neurons with variable activity in one hidden state (i.e. highly selective). All the other elements of the matrices were set to 0. The second block contained matrices with two random elements per row in the range [0,1] and the other set to 0,

while the third block contained matrices with all the elements different from 0. Probabilistically, these 3 blocks of synthetic emission matrices simulated 3 different neural populations with the 1/3 (33.3%), 2/3 (66.7%) and 3/3 (100%) of the units active during each state. We computed the Gini coefficient on all the matrices to obtain 3 reference distributions of synthetic values. Note that for the Gini coefficient analysis performed in the 2-state HMMs case, we generated 2 blocks of synthetic [100 neurons x 2 states] emission matrices by the same logic applied in the 3-states HMMs case.

3.3.5 Comparisons between state sequences

To compare two different state sequences decoded by the HMM algorithm and characterized by T bins and N states, we obtained two numeric vectors with N x T elements concatenating the probability of the N states for each sequence. We then computed the R^2 between the two vectors as a measure of their similarity (values near 1 meaning that the two curves perfectly match).

Based on this measure, we developed a procedure to test if the two sequences of interest were significantly different or not. Starting from the trained models (real models) that had produced the state sequences of interest (real state sequences), we generated 200 new state sequences (100 fake state sequences for each model to compare) shuffling the emission matrices of the real models along the columns (states). Note that by shuffling training models we obtained biologically plausible fake models (i.e. with plausible probabilities to observe spikes from the cells) assigning to one neuron the probability to discharge in the same state of a different neuron (randomly chosen without repetition). We then computed a Gaussian null distribution calculating the R^2 between each of the real state sequences and the fake sequences. The null distribution represented the reference values of the R^2 for different sequences (real vs randomly generated). We considered the two real sequences as not significantly different if their R^2 was higher than the null distribution (Z-test, $p<0.05$).

3.4 Sliding window t-test

To examine whether the results obtained with the HMM were present also at single cells, we performed a sliding window t-test analysis. We repeated the same procedure within different temporal intervals. Basically, we used the same temporal intervals of interest where we had applied HMM and we took a fix time window as reference. This fixed time window coincided with one of the average hidden states detected, thus its time width depended on the mean duration of the state. For each cell, we then performed a series of t-tests ($p<0.05$) between the firing rate computed in the fixed time window and the firing rate computed in a sliding window of equal width that moved in 10-ms steps. For each step, we calculated the percentage of the cells in the population that showed a significant

change in firing rate with respect to the fixed window (mean and standard deviation of 5000 bootstrap samples). As a control, we repeated the procedure taking as reference an initial and a final 300 ms window that extended from -1000 to -700 and from +700 to +1000 ms with respect to movement onset, respectively (Figure 16).

3.5 Neural trajectories

We projected the high-dimensional data on a reduced 3D-space using a standard Principal Component Analysis (PCA). We analysed recordings starting 1000 ms before movement onset and ending 1000 ms after. Since neural data were not recorded simultaneously, we aligned the data across different trials assigning a fixed number of bins to each of the main behavioural epochs (Delay, 370 bins; Reaction time, 130 bins; Movement, 190 bins; Hold, 310 bins) such that the total number of bins was 1000 and the average bin width was ≈2ms. We then smoothed (Gaussian filter, sigma ≈ 110 ms) the binned spike trains for each trial separately and computed the condition averages. With these data, we built a [m x n] matrix where m = N° of cells and n = N° bins * N° conditions; we normalized in the range [0,1] along the rows to avoid high firing rate units to excessively influence the analysis and we then performed the PCA on the pooled neural data.

To investigate the temporal evolution of population activity within each hidden state, we fragmented the 3D - neural trajectories averaged across trials of the same condition in 6 segments, one for each hidden state (DELAY, PREMOV, ACC, DEC, EARLY HOLD, HOLD) obtaining 54 segments in total (6 states * 9 conditions). Each segment was resampled at 20 equally spaced points and the centroid of each segment was aligned with the origin of the axes. We computed the mean Euclidean Distance between all the points (20) of segments belonging to the same state (intra-state distance) or belonging to different states (inter-state distance): lower distances meant similar segments shapes (i.e., similar temporal evolution of the neural trajectory segments).

4 Results

Our dataset consisted of neurons recorded from two areas, namely V6A, located in the anterior bank of parieto-occipital sulcus and PEc, in the adjacent caudal sector of medial PPC (Figure 7a). Data were collected from two monkeys (M1 and M2) trained to perform an instructed delay reaching task towards visual targets (light emitting diodes, LEDs) located in 9 different positions (3 directions x 3 depths), placed at eye level (Figure 7b).

The animal sat on a primate chair in complete darkness and pressed a home button (HB) to begin the trial. Randomly, one of the LEDs was switched on and monkey had to fixate its gaze on it. After a variable delay, the LED changed colour and this cued the animal to perform an arm reaching movement and hold the reached position. After a variable period, the LED turned off and the animal moved its arm back to the HB position to receive reward (Figure 7c). Movement onset was defined by the release of the HB, as detected by the embedded microswitch (1ms resolution). Movement end was measured as activation of a microswitch positioned on the target.

Cells with activity recorded for 10 correct trials for each target were used for analysis, without any further preselection. Data from different recording sessions were pooled together to construct four neural ensembles (2 animals x 2 areas) that were analyzed with population methods. Neural ensembles consisted of 104 and 93 units from V6A and PEc, respectively in monkey M1; 105 and 83 neurons respectively, from V6A and PEc in monkey M2 (see Figure 8a for the recording sites).

Figure 7d shows a simple scheme of an HMM. In this view, a neural population goes through a chain of hidden states that makes each unit discharging with different probabilities. The transition matrix contains the probability to switch from each state to another, defining the topology of the Markov process. The emission matrix in turn, estimates the probability to observe a spike from each neuron in each state and it represents the link between the recorded neural activity and the unobservable sequence of hidden states. Like any machine learning method, an HMM involves a training step to estimate the optimal parameters of the model i.e. the transition and the emission matrices and the subsequent decoding on a test data set (Figure 7e). Then, given an observed spike train, we used the estimated model to infer the probability at each time instant to be in one of the possible states (i.e. the state probability sequence or state sequence, Figure 7e). We converted the spike counts in emission sequences and we cross-validated every model to ensure the predictive capacity of our model (see Methods).

4.1 'Macro' neural states corresponded to main task phases

A crucial problem in HMMs is the definition of the optimal number of hidden states that represent the different patterns of activity. We addressed this issue with two different approaches while analyzing a time interval spanning from 1000 ms before the arm movement start until 1000 ms after to include the main behavioural events of the task.

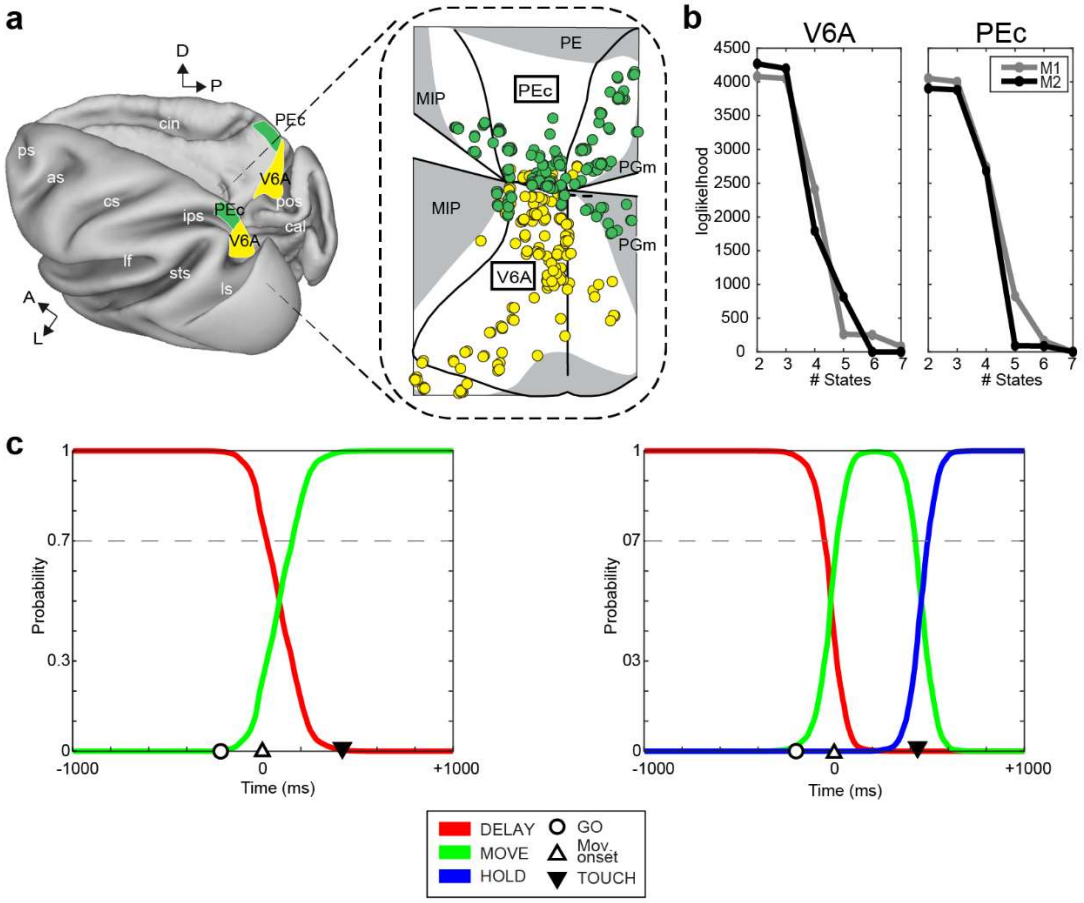

Figure 8. a) Recording sites in V6A and PEc. 3D reconstruction of macaque brain and 2D flattened map of the two areas. Same conventions of Figure 7. Penetrations spread to cover almost entirely the surface of the two areas. b) Average log-likelihood for HMMs with an increasing number of states. The profile of log-likelihood is consistent with the consistency analysis and, in particular, three is the optimal number of states to represent the population activity (more detailed model with high likelihood). c) An example of state sequence decoded by 2-state and 3-state HMMs. Colored lines represent the time course of the probability of each state. Horizontal dashed line: threshold set at 0.7 of probability. The second and third states (MOVE and HOLD) of the 3-state HMM merge into a single second state in the 2-state HMM. From Diomedi et al. 2021.

First, we checked the consistency of different numbers of states. For this analysis, we trained HMMs with different numbers of states (from 2 to 7), then we used the trained models to decode each testing sequence, obtaining each time a different state probability sequence. A state sequence decoded by a *N*-states model was defined 'consistent' if the algorithm detected *N* hidden states with a probability

above the threshold. Optimal was the number of states that decoded the highest percentage of consistent sequences in the testing dataset (see Methods).

Figure 9a shows the percentage of the emission sequences in which 2, 3, 4, 5, 6 or 7 neural states were consistently decoded. In both areas, 2 and 3 states were detected in the 100% of the emission sequences in both animals; 4 states were present in about the 60% of the sequences (M1: 59% and 68% in V6A and PEc, respectively; M2: 42% and 69%). Adding more states, the percentage of consistency further decreased. According to the percentage of consistent decoded sequences, both 2 and 3 (scoring a consistency of 100%) could be considered as the optimal number of states.

The second approach was to compare the goodness of fit (estimated as log-likelihood) of the models trained previously (Figure 8b). The HMM with the optimal number of states should have the highest log-likelihood. In agreement with the consistency analysis, the models with 2 and 3 states had the highest log-likelihoods. In addition, after visual inspection of the data it was evident that the states decoded by 2-state models could result from 3-state models by merging two adjacent states (the first with the second or the second with the third, depending on the sequence; see Figure 8c). Given this, we chose 3 -instead of 2- as the optimal number of hidden states for the subsequent analyses. Figure 9b shows the average state probability sequence of 3-state HMMs trained separately for each target position. Comparing across areas (Figure 9b, left and right panels) and animals (Figure 9b continuous and dashed line), showed that the probabilities and timing of the activity patterns were quite similar. An initial state was present from the start of the analysis window (red lines) and its probability sharply decreased about 50 ms before arm movement onset. Around this time, a second state (green line) emerged and was present for ~0.5 sec, until the end of movement. After that, a third state (blue line) rose and lasted until the end of the analysis window. The thin shaded areas shown in the figure indicated a high consistency across trials of the state sequence probability (see also the little variability of state transition timing below). To measure the similarity of the state probability sequences across animals and areas, we computed the R^2 between them. The R^2 values were compared against a null distribution of synthetic shuffled data (see Methods). The state sequences were not statistically different in all the possible comparisons with R^2 values higher than 0.95 (see Table S1). The timing of these three states coincided with the main task epochs i.e. waiting for the 'go' signal, moving the arm towards the target LED and holding the target. Accordingly, we named these 3 hidden states after the main task epochs as DELAY, MOVE and HOLD.

To evaluate in finer resolution the timing of transitions between the three hidden states and compare it across animals and cortical areas, we applied a threshold (0.7, black dashed line in Figure 9b). Each transition included the 'fall' of one state (probability<0.7 threshold) and the 'rise' of the subsequent

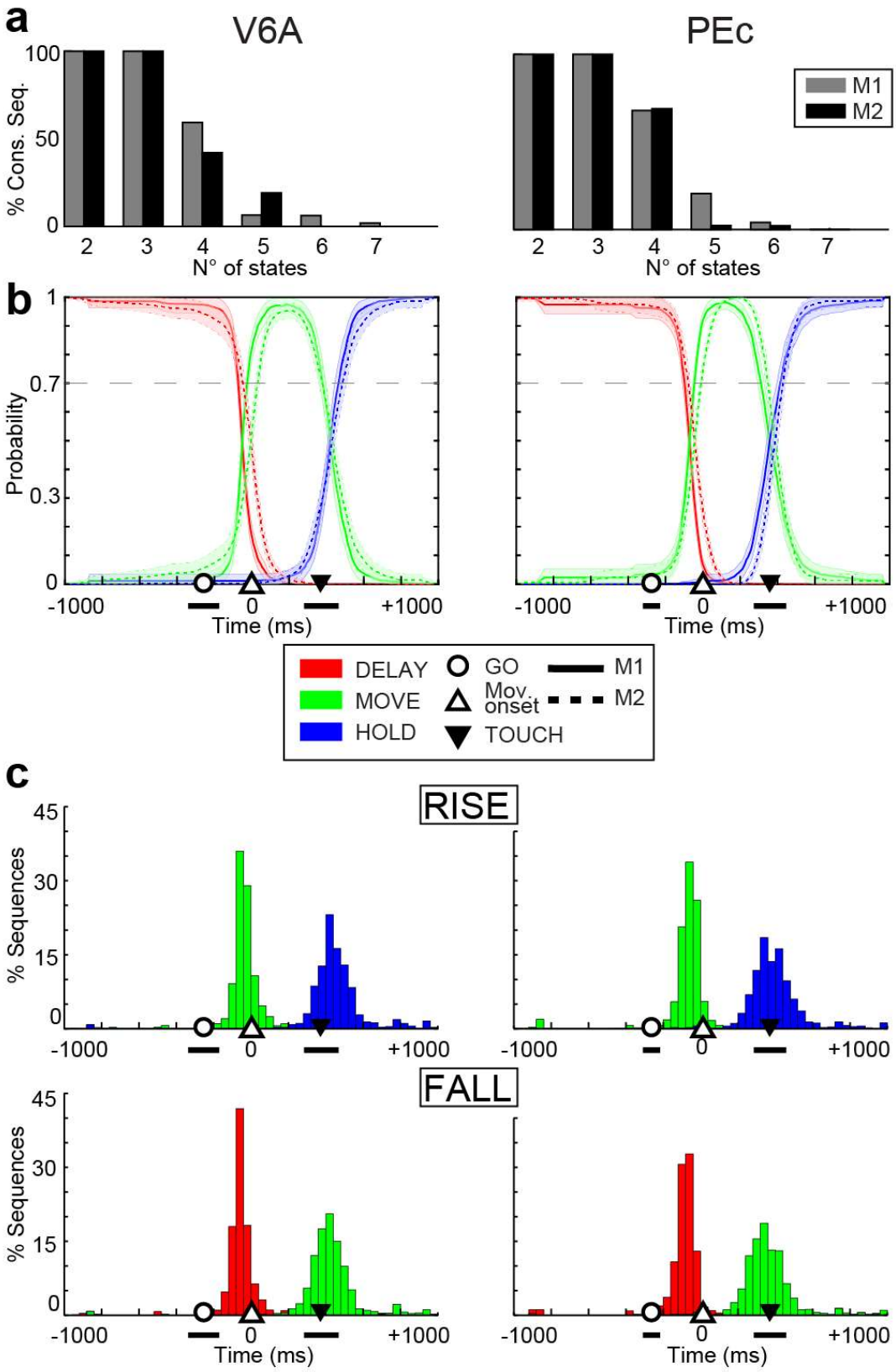

Figure 9. Consistency analysis and results for 3-state HMM. a) Bars indicate the percentage of sequences in which was possible to find a different number of neural states (2-7). We found that 3 was the highest number of states detectable in almost all the sequences. b) Average state sequences for 3-state HMMs. Colored lines (continue for M1, dashed for M2) represent the time course of the probability of each state. Shaded areas: ± S.E.M. across trials. X-axis: time (2ms-bin);

y-axis: probability. Symbols: timing of main behavioural events averaged across trial and positions. Black thick lines under symbols: variability of event timing (mean ± S.D). Horizontal dashed line: threshold set to identify 'active' states (0.7). The model individuated 3 different neural states along the trial highly consistent across animals and areas. c) Timing of state rises (i.e., when its probability exceeded the threshold) or falls (when vice versa its probability fell above the threshold). Y-axis: the frequency expressed as percentage of emission sequences. Every column of the histogram has a temporal resolution of 40 ms (20 bins). Symbols: timing of main behavioural events averaged across trial and positions. Black thick lines under symbols: variability of event timing (mean ± S.D). The distributions of rises / falls indicate that the switches between one neural state and another were tightly related to main behavioural events. From Diomedi et al. 2021.

state (probability>=0.7). Figure 9c shows the rise and fall distributions, separately for each area (pooling together data from the two animals). In all transitions, the distributions of 'fall' of one state and 'rise' of the subsequent overlapped extensively. Importantly, the distribution peaks fell remarkably close to the behavioural events. In V6A and PEc the state DELAY ended at -60 ±146 (mean ± S.D.) and -89 ±129 ms, respectively relative to movement onset, whereas the state MOVE rose in V6A and PEc at -28 ± 142 ms and -59 ± 130 ms, respectively, always in relation to the same event. With regards to the movement end, the state MOVE fell in V6A and PEc at 45 ± 145 ms and 0 ± 125 ms, respectively, whereas the state HOLD rose at 78 ± 145 ms and 32 ± 124 ms, respectively for V6A and PEc. Comparing the 2 areas, we observed statistically significant differences in timing, with PEc leading V6A by 38 ms on average (Wilcoxon test, $p<0.05$, see Methods). Moreover, since the timing of the behavioural events could vary on a trial-by-trial basis, by correcting for this variability, we further reduced the variability of the state transitions (i.e. variability across states after the correcting for behavioral markers variability) to a range that spanned from a minimum value of 33 ms to a maximum of 62 ms.

4.2 Emission matrices reveal the sustained response of neurons over multiple neural states

For each state and neuron, the model estimated a value between 0 and 1 that quantifies the probability to observe a spike from that neuron during a given state and this information was collected in the emission matrix.

Figure 10a illustrates the emission matrix averaged across targets, with rows corresponding to the various states and columns representing neurons, with the color intensity being proportional to their activity. Neurons were sorted in descending order of state selectivity measured as the variance of the emission probability vector.

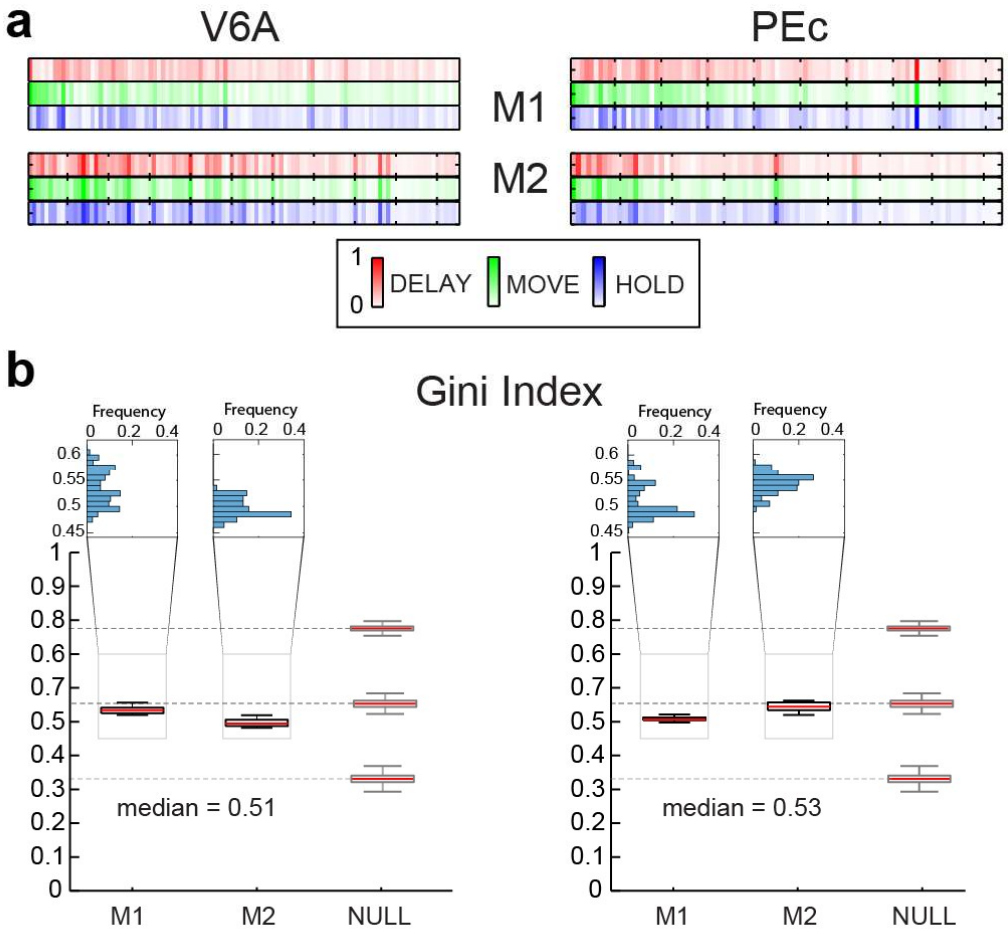

Figure 10. Single cell contribution to the neural states. a) Graphical representation of the emission matrices averaged across positions. Cells (columns) are sorted in descending order (left to right) based on the variance of the probability to fire a spike in each state. The cells selective for one/two states are shown on the left part of each matrix and nonselective cells are shown on the right part. b) Gini Index calculated on the emission matrices for V6A (left) and PEc (right). The index computed on the real data is compared with the index computed on synthetic data (NULL). In each boxplot, the median and the 25th and 75th percentiles, respectively, are shown. The whiskers extend to the most extreme data points not considered outliers. All the 4 populations have Gini Index not different from that of a synthetic population in which, during each neural state, the 2/3 of the cells are active. The inserts at the top show in detail the distributions of the Gini indexes computed on the real data. From Diomedi et al. 2021.

To test whether the hidden states relied only on the neurons with high state selectivity (high variance) or, conversely, on the entire population, we trained an additional set of HMMs excluding from the population 10% of the most state selective neurons (the units on the left of the matrices shown in Figure 10a, see Methods). The state sequences decoded by these 'reduced' HMMs (Figure 11) were very similar to the ones decoded by the 'complete' HMMs (Figure 9b), suggesting that the different activity patterns included the whole population and not only the cells tuned selectively for certain states. Indeed, the R^2 between the 'reduced' and the 'complete' state sequences resulted to be very highly correlated (see Table S2 in the Supplementary Material).

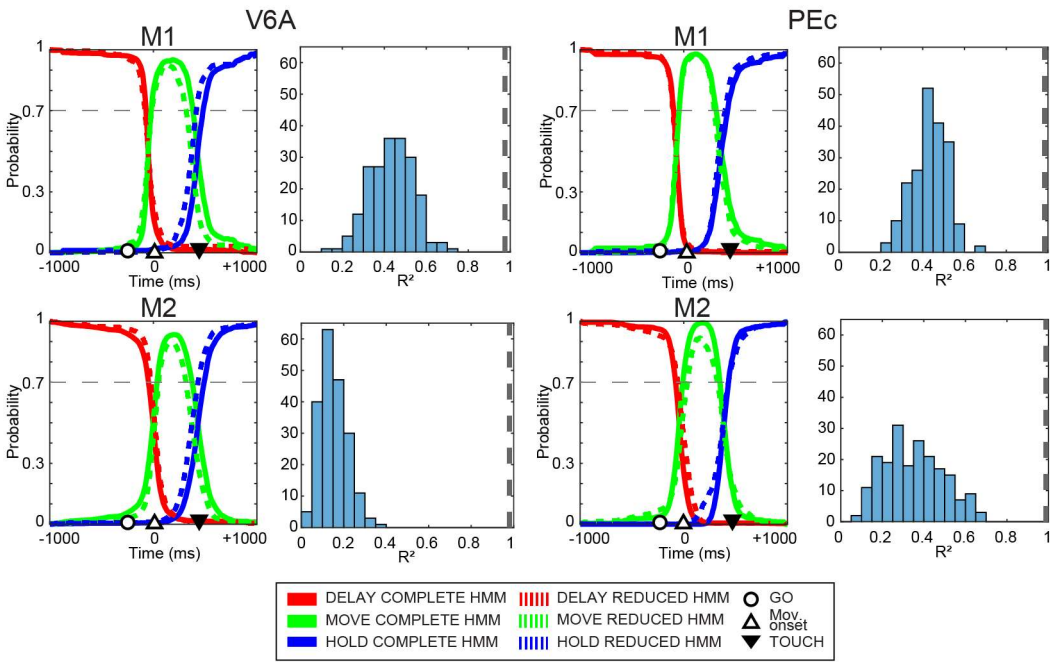

Figure 11 . Comparison of average state sequences for 3-state HMMs that use data from the entire population ('complete HMM') vs after the removal of the 10% of cells more strongly modulated between the neural states ('reduced HMM'). Colored lines (continue for complete models, dashed for reduced) represent the time course of the probability of each state. The average position (across trial and positions) of the main event markers is shown (inset). Horizontal dashed line: threshold set at 0.7 of probability. Vertical dashed line represents R2 of the comparison between complete HMM and reduced HMM. The hidden states arise from the entire population, thus after removing the more selective cells the same neural states are still clearly identified. From Diomedi et al. 2021.

We further investigated the relation between neural states and single unit activation by computing the Gini coefficient on the emission matrix (Maboudi et al., 2018). The Gini index ranges between 0 and 1 and measures the sparsity of a matrix. A high Gini index ($\simeq$1) indicates that neural states strongly activate a few units. Conversely, a low Gini index ($\simeq$0) shows that the entire population is active in each neural state. Figure 10b shows the median Gini index in the 4 neural populations and the median Gini index value of synthetic populations composed of cells with high, medium and low state selectivity (see Methods). The Gini values for the real data were very similar to a synthetic population with a median Gini index equal to 0.55 constructed with the assumption that the 66% (2/3) of cells were active during each state. Note that, computing Gini index for the 2-state HMMs, we have obtained a median value equal to 0.5 which is between the Gini coefficient computed on the first synthetic population whose neurons discharge only for a state (0.66) and the Gini coefficient computed on the synthetic population whose neurons discharge for each state (0.33). This showed that the previous result holds true for two states models and also in this case, they cannot be encoded by 2 separate subpopulations. Furthermore, this highlights that overlapped populations were not the result of forcing the model to search for additional states.

4.3 HMMs in restricted time windows revealed several 'micro' states

For simplicity, we will refer to the 3 neural states before mentioned as 'macro' states because they were detectable in all the analyzed emission sequences considering a large temporal window (2000 ms, centered on movement onset). Our analyses so far were based on the 3-state model; however, 4-state models also provided a high consistency of decoding (Figure 9a). In 4-state models, the 3 'macro' states described previously were still detected and in addition a fourth state popped up either between DELAY and MOVE, or between MOVE and HOLD states (Figure 12).

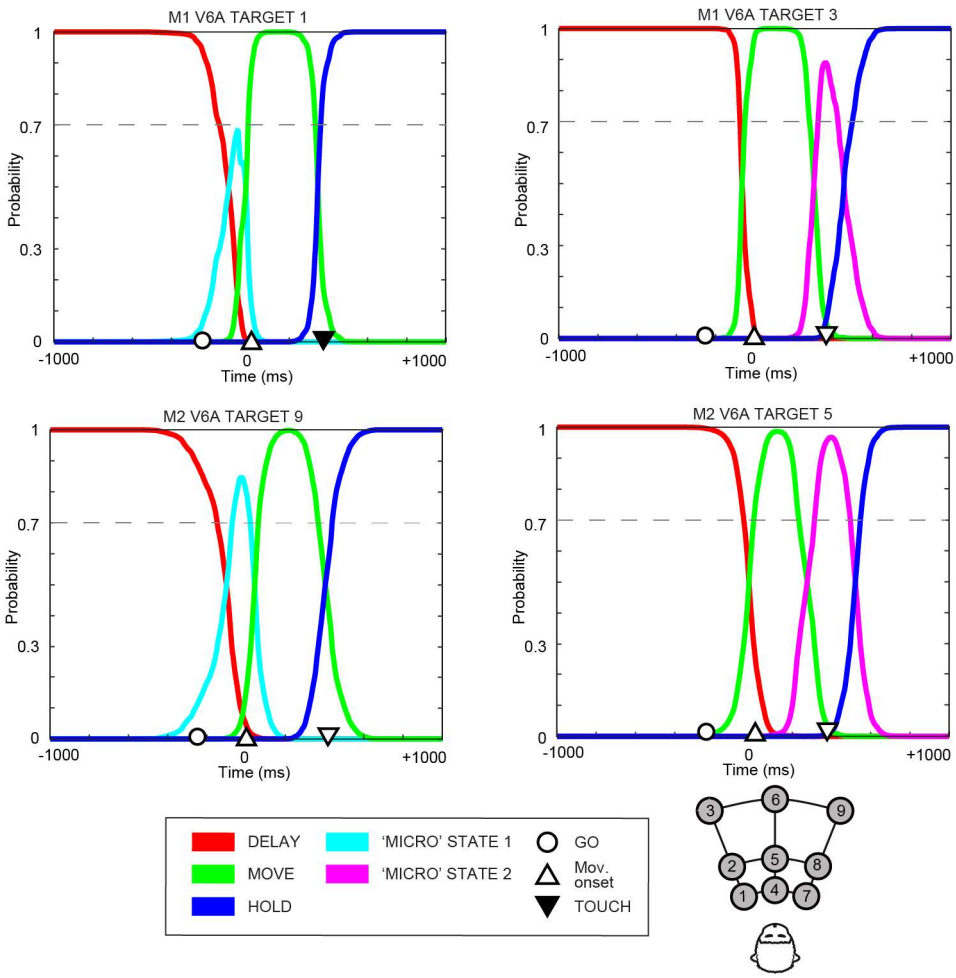

Figure 12. Average state sequences for 4-state models. Same conventions as Figure. 9. The sequences on the left show a brief neural state that extends within the reaction time of the animal (PREMOVE micro state; cyan lines). The sequences on the right show a neural state that reached its peak levels when the animal touched the target (EARLY HOLD micro state, magenta lines). From Diomedi et al. 2021.

To investigate these additional states, we analyzed the timing of the transitions decoded by the 4-state models (see Methods). We found that all the six distributions (falls of states 1, 2 and 3; rises of states 2, 3 and 4) significantly deviated from unimodality (Hartigan's Dip test for unimodality, $p<0.05$).

This finding was consistent with the existence of two additional minor states rather than a single fourth 'macro' state. To further investigate these two minor neural states, we then focused our analysis on smaller time windows. Before moving on, please note that we defined as 'micro' states these additional minor neural states that were decoded from only a fraction of the emission sequences and that required narrower ad hoc time windows to be properly studied.

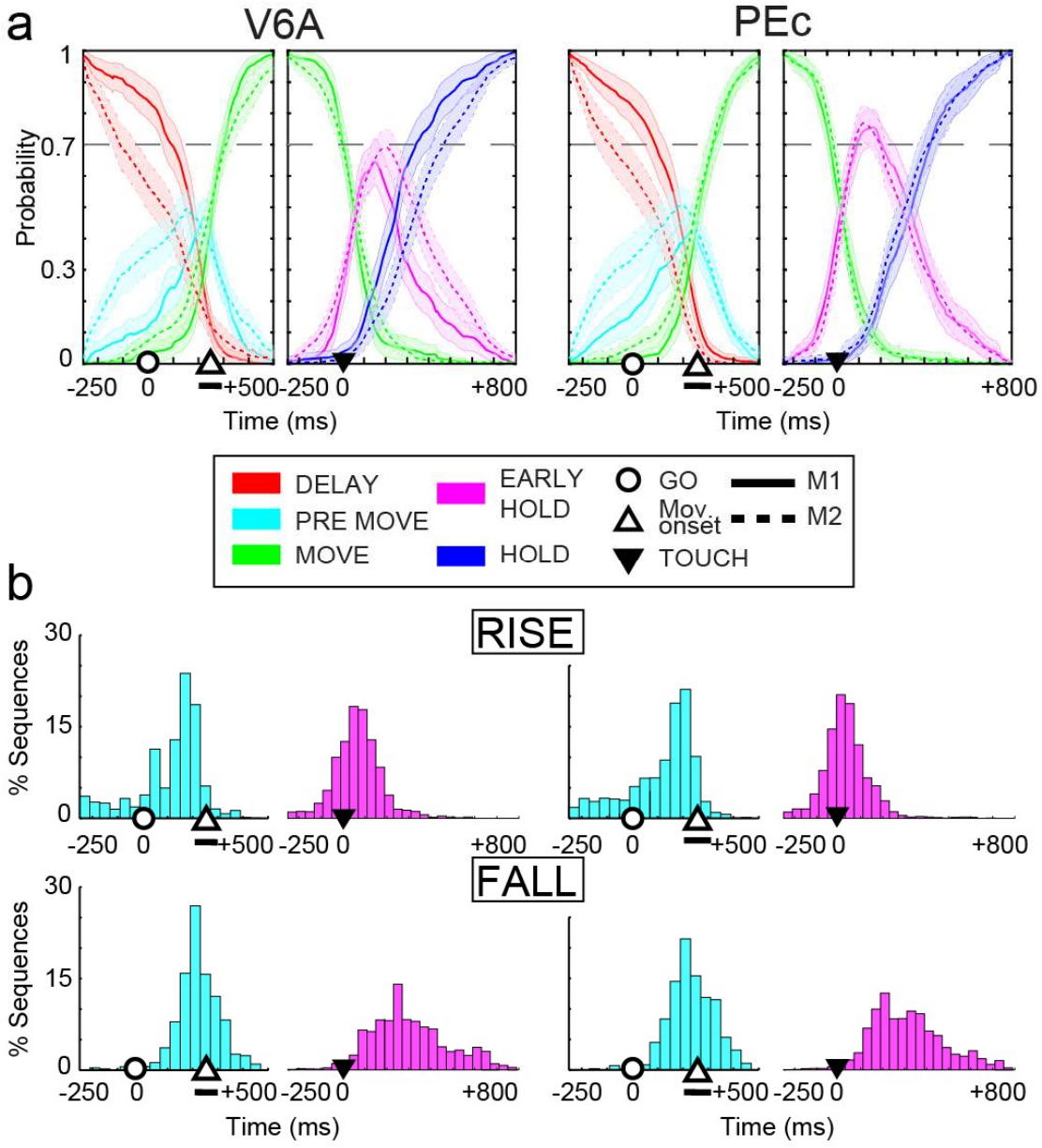

Figure 13. 'Micro' states revealed by applying HMM in restricted time windows. a) Average state sequences for 3-state HMMs separately trained on two periods, one from 250 ms before to 500 ms after the 'go' signal and the other from 250 before to 800 ms after movement end. Two 'micro' states emerged during movement reaction time and during the first 250 ms after the movement end. Same conventions as in Figure 9. b) Timing distributions of 'micro' states rises or falls. Same conventions as in Figure 9. From Diomedi et al. 2021.

Regarding the first 'micro' state that appeared between DELAY and MOVE, we examined whether it could be related to the 'go' signal event and the preparation of the upcoming movement. Thus, we aligned discharges at this event and trained a 3-state HMM on a temporal window spanning from 250 ms before until 500 ms after. Figure 13a (cyan color) shows that the probability of this state was lower than the 'macro' states (0.53 and 0.49 at the peak for V6A and PEc, respectively), but it could be still decoded in the majority of sequences (M1: 57% and 66%, V6A and PEc respectively; M2: 46% and 62%; see Methods). Note that the state probability shown in Figure 13a is the average of all individual state probability sequences with 3 states which passed the threshold (0.7). Due to the fact that the individual states crossed the threshold at variable time points, the peak of their average could appear globally lowered and below threshold. Moreover, the averaged state sequences were similar across areas and animals ($R^2 > 0.80$; Z-test, $p < 0.05$; see Table S1 for all R^2 values and null distributions). This first 'micro' state emerged 68 ± 154 ms after the 'go' signal and disappeared at 28 ± 102 ms before movement onset in V6A. In comparison, in PEc the corresponding values were 70 ± 152 ms and 34 ± 104 ms (Figure 13b cyan histograms). After accounting for the variability of the movement onset, the timing uncertainty of this 'micro' state fall ranged from 36 to 52 ms . These results suggest that a distinct activity pattern was present in both areas during the movement reaction time that we hereafter refer to as PREMOVE, thus providing evidence for short-lead movement preparation signals in parietal ensemble activity.

To probe for a 'micro' state also between MOVE and HOLD states, we aligned activity at the movement end event and analyzed a window from 250 ms before until 800 ms after. This window was selected in order to supply the model with enough data to correctly detect possible 'micro' states. Figure 13a (magenta curves) shows the averaged probability of this state across time, with maximum probability being higher than PREMOVE state (0.70 and 0.79, respectively for V6A and PEc) and it was detected in a higher number of sequences (M1: 69% and 82%, V6A and PEc respectively; M2: 65% and 74%; see Methods). The decoded state sequences were similar across animals and areas ($R^2 > 0.90$; Z-test, $p < 0.05$; see Table S1 for all the values). This 'micro' state rose at 77 ± 131 ms and fell at 314 ± 184 ms after movement end in V6A, while in PEc the corresponding values were 35 ± 109 ms and at 314 ± 166 ms (Figure 13b magenta histograms). These findings further substantiated the presence of another 'micro' state that was active during the first 250 ms of holding the target period and thus we will refer to it as EARLY HOLD state.

4.4 'Micro' states during movement were related to distinct movement phases

Lately, it has been reported that HMMs divided the motor cortex activity during arm movement into two states temporally coupled to the two acceleration and deceleration phases of the arm (Kadmon

Harpaz et al., 2019). Prompted by this finding, we examined the possibility that a similar movement decomposition could be detected also in parietal cortex ensemble activity, given that so far single-cell and population parietal activity were reported to encode movement parameters like direction or trajectories (Mulliken et al., 2008b; Torres et al., 2013).

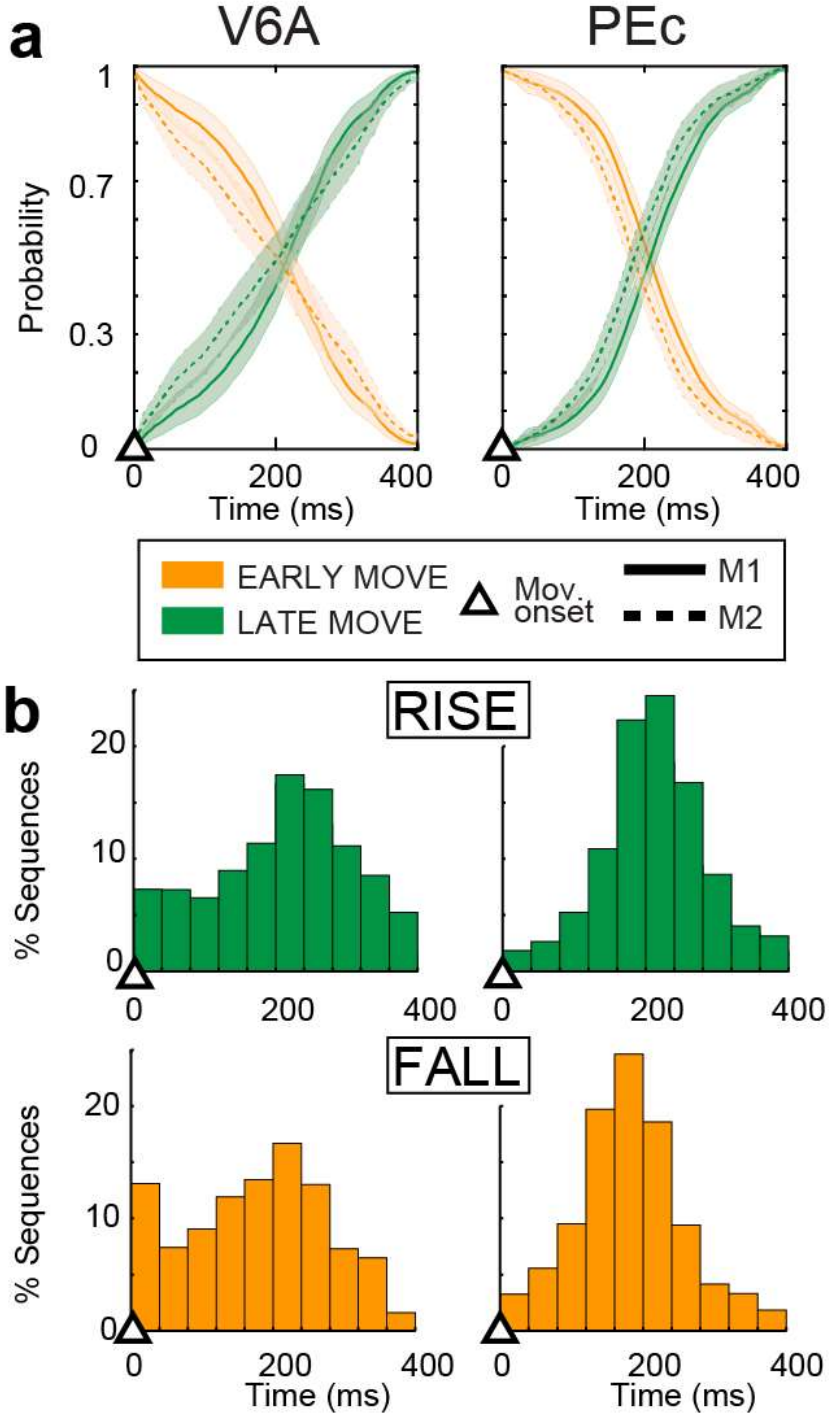

Figure 14. Segmentation of population activity during movement in two 'micro' states. a) Time course of average state sequences of 2-state HMMs. Activity from movement onset to 400 ms after it were analysed. The transition occurred halfway along the movement. Same conventions as in Figure 9. b) Timing of state rises or falls. Same conventions as in Figure 9. From Diomedi et al. 2021.

HMMs were trained to search for two states during movement, starting from its onset until 400 ms after, to include the average movement time. Rather unexpectedly for two parietal areas, two states emerged (Figure 14a) in the vast majority of sequences (M1: 88% and 80% in V6A and PEc, respectively; M2: 72% and 91%; see Methods) and the decoded state sequence was consistent between animals and areas ($R^2 > 0.90$; Z-test, $p < 0.05$; see Table S1). We refer to these two subsequent 'micro' states as 'EARLY MOVE' and 'LATE MOVE' (see Discussion for further details on their functional meaning). Even more importantly, the transition between these two states occurred halfway through the analysis window (Figure 14b) (EARLY MOVE fall: 175 ± 99 and 180 ± 74 ms after movement onset; LATE MOVE rise: 207 ± 99 and 211 ± 72 ms in V6A and PEc, respectively). To examine whether these two states were a model artifact, the R^2 between the real state sequences was compared against a null distribution of synthetic, random state sequences and found to be significantly different (Z-test, $p<0.05$). This confirmed that the EARLY and LATE MOVE states were not an artifact but reflected real neural processes. In sum, using HMMs the parietal population activity during the movement was decomposed into two different 'micro' states that very likely reflect the different phases of arm movement (see Discussion).

4.5 Single cell modulations related to 'macro' and 'micro' hidden states

We subsequently tested whether the ensemble activity changes underlying the hidden states and their transitions were present in single neurons. Thus, for each cell, a series of t-tests was performed to compare the firing rate within a fixed window with the firing rates computed in a sliding window of equal duration that moved in 10-ms steps, starting from 1 sec before movement onset until 1 sec after. At each step the percentage of cells with activity significantly different (t-test, $p<0.05$) between the two windows, was computed. First, we chose as fixed window the time interval that corresponded to the mean duration of MOVE state (from movement onset until 400 ms after). The sliding window spanned from 1000 before movement onset to 1000 after it. As illustrated in Figure 15a, we observed a significant drop in cell modulations, occurring around the DELAY-MOVE state transition and a sharp increment during MOVE-HOLD switch. Thus, the incidence of single-cell activity modulations matched the three 'macro' states temporal evolution (Figure 15a). In sum, the majority of neurons ($\simeq$ 70%) changed their firing twice along the trial, thus giving rise to the ensemble activity patterns that were detected by the 3-state HMMs. As a control, we repeated the same procedure taking as reference windows one time interval that included the first 300 ms of delay epoch and another interval at the end (hold epoch) of the temporal window considered for the analyses (see Methods).

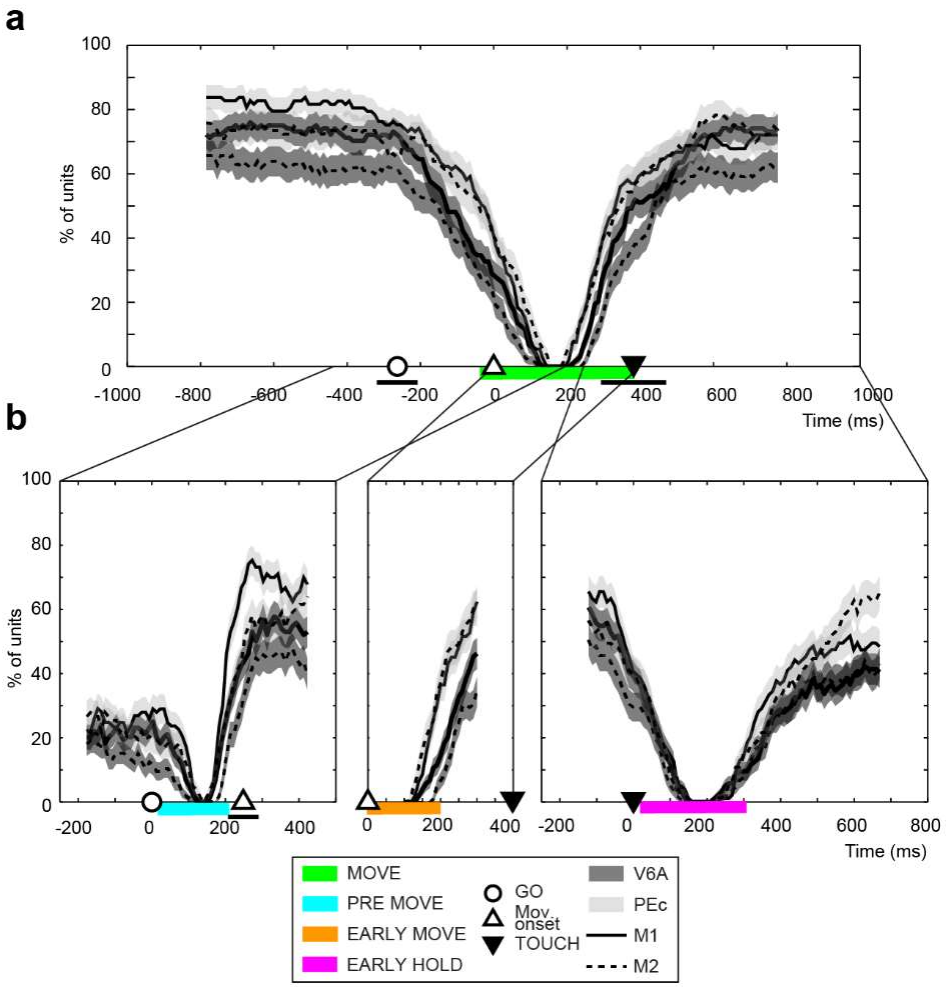

Figure 15. Single cell modulations underlying population activity neural states. a) Percentage of units with significantly different (t-test, $p<0.05$) firing activity between a fixed window (colored bar below the x-axis corresponding to the mean MOVE neural state) and a sliding window of equal duration (step: 10 ms). Neural data were aligned at movement onset and analyzed from 1000 ms before this event until 1000 after. Shaded areas on the curves illustrate the bootstrap standard deviations. Two sharp change points (-200 – 0 ms and 200 – 400 ms) separate more horizontal segments of the curve and coincide with the transitions between the 3 'macro' neural states b) Percentage of cells with activity changes at the time points around the transitions between the several 'micro' states. Same conventions of Figure 15a. Curves show steep change points in correspondence with transitions between the different 'micro' neural states. From Diomedi et al. 2021.

Figure 16 shows the results with the two curves superimposed to highlight the abrupt changes in single cell modulations that corresponded to those observed in Figure 15a. This finding strongly supports that the sharp neural changes were not an artifact, or a bias of the analysis used but underlying neural dynamics.

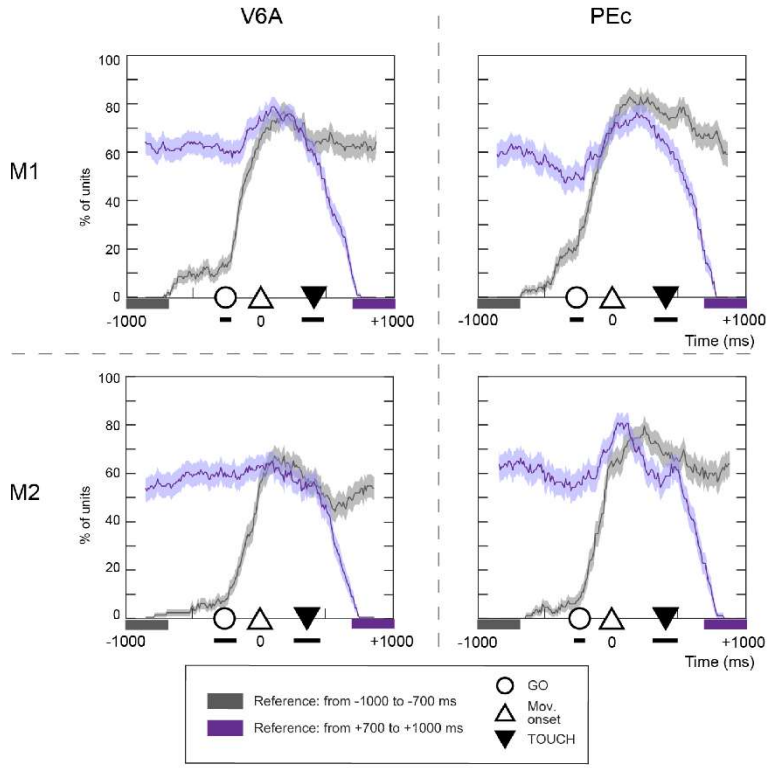

Figure 16. Single cell modulations underlying population activity neural states. The curves show the percentage of units with significantly different (t-test, $p<0.05$) firing activity between a fixed 300 ms window (colored bars below the x-axis) and a sliding window of equal duration (step: 10 ms). Neural data were aligned at movement onset and analyzed from 1000 ms before this event until 1000 after. Shaded areas on the curves illustrate the bootstrap standard deviations. From Diomedi et al. 2021.

To investigate also the relationship of single cell modulations with the several 'micro' states, we performed three additional sliding t-test analyses using as fixed windows the PREMOVE, EARLY MOVE and EARLY HOLD states, respectively (Figure 15b). Accordingly, in each of these analyses the sliding window spanned the same period used to identify the corresponding 'micro' state.

Across these tests, we observed that the firing rate of about 25-60% of the population was significantly different before and after the 'micro' states transitions. In particular, within the movement phase we found that 35-60 % of units significantly changed their firing rates (Figure 15b middle; see Figure 17 for cell examples). In conclusion, we observed that the 'macro' and 'micro' states of the population activity were linked to single cell modulations.

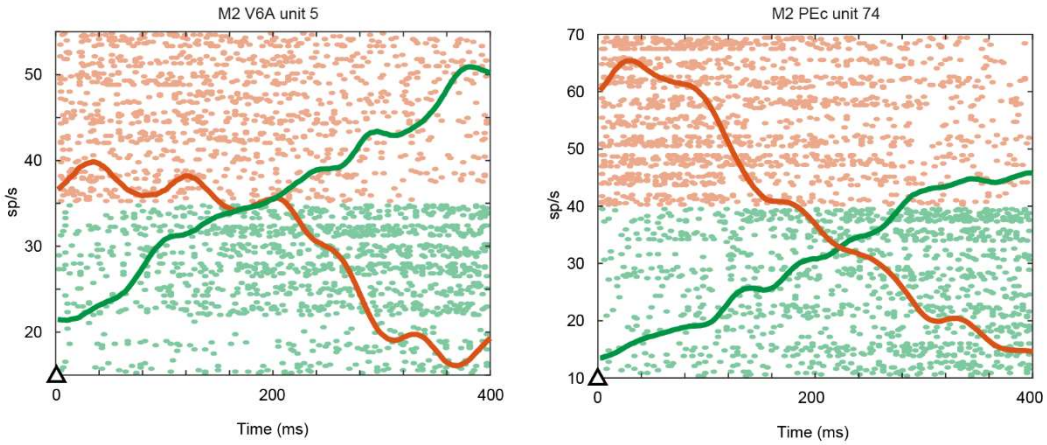

Figure 17. Examples of neurons modulated in EARLY and LATE MOVE neural states. The time window spanned from movement onset to 400 ms after it. Spike trains for all 90 trials (9 targets x 10 repetitions) are reported. Continuous lines represent the average firing rate. Red: units with high activity during the EARLY MOVE state. Green: units with high activity during LATE MOVE phase. Left: neurons from V6A. Right: neurons from PEc. From Diomedi et al. 2021.

4.6 Temporal evolution of population activity within HMM states

To fully examine the complexity of population dynamics, we performed a principal component analysis (PCA, see Methods) and projected the ensemble activity into a low-dimensional space defined by the first 3 principal components. Figure 18a shows example neural trajectories of the population activity recorded from V6A (left) and PEc (right) in M1 and M2, respectively (see Figure 19 for other examples). In both examples, 9 smooth neural trajectories clearly separated from each other were obtained by applying PCA on the condition averaged firing rates (see Methods). Note that the reach goal position was cued before the start of the analysis window, so the trajectories differed between targets from their beginning. In Figure 18a and 19, on each trajectory the averaged HMM states are indicated with different colours.

It should be noted that the first 3 Principal Components (PCs) accounted for a significant fraction of the variance in the neural data (M1: V6A [21%+15%+12%=48%], PEc [25%+16%+ 10%= 51%]; M2: V6A [16%+12%+9%=37%]; PEc [22%+18%+ 9%=49%]).

Interestingly, the EARLY MOVE-LATE MOVE switch occurred at a turning point in population activity halfway between movement onset and target touch, thus confirming a significant change in cells' discharges within the reaching phase (see colours in Figure 18a and 19 and Discussion for more details).

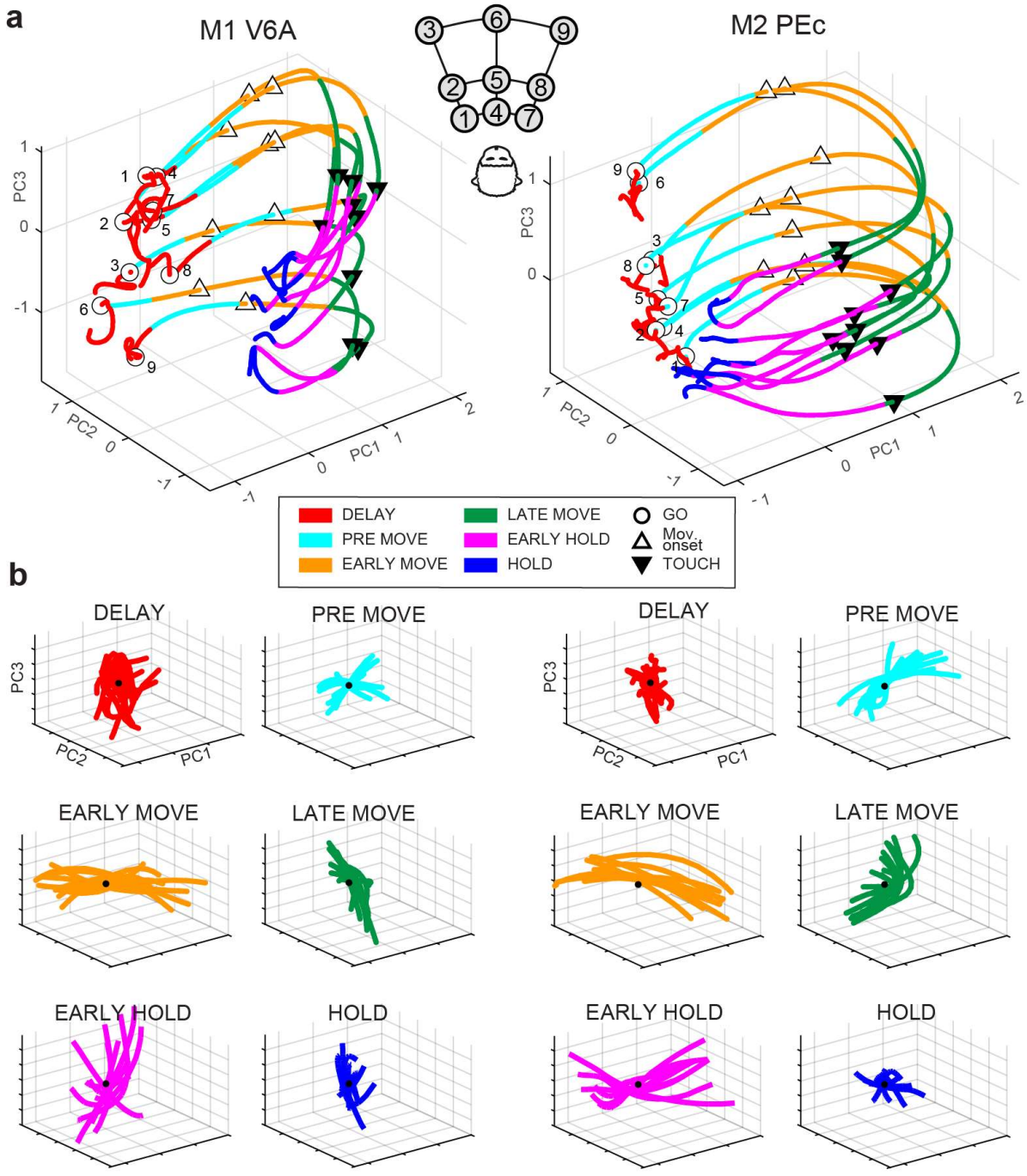

Figure 18. Neural trajectories and their HMM-based segmentation. a) Neural trajectories averaged across trials relative to each target position (location, see legend above) plotted in the 3 first PC's space (left panel: M1 V6A; right: M2 PEc). Different colours correspond to HMM states. Behavioural events: instruction onset (white circle), onset of the movement (white upward triangle) and start of the hold phase (black downward triangle). The population activity for different targets is clearly segregated in the 3D space, but it shows similar evolution in the 9 conditions. The first 3 PCs explained 37-51% of the total variance. b) Segments of neural trajectories cut following the hidden state transitions and with centroids aligned. Same colour code than Figure 18a). The segments of population activity associated with the neural states show characteristic temporal dynamics that are different from state to state. From Diomedi et al. 2021.

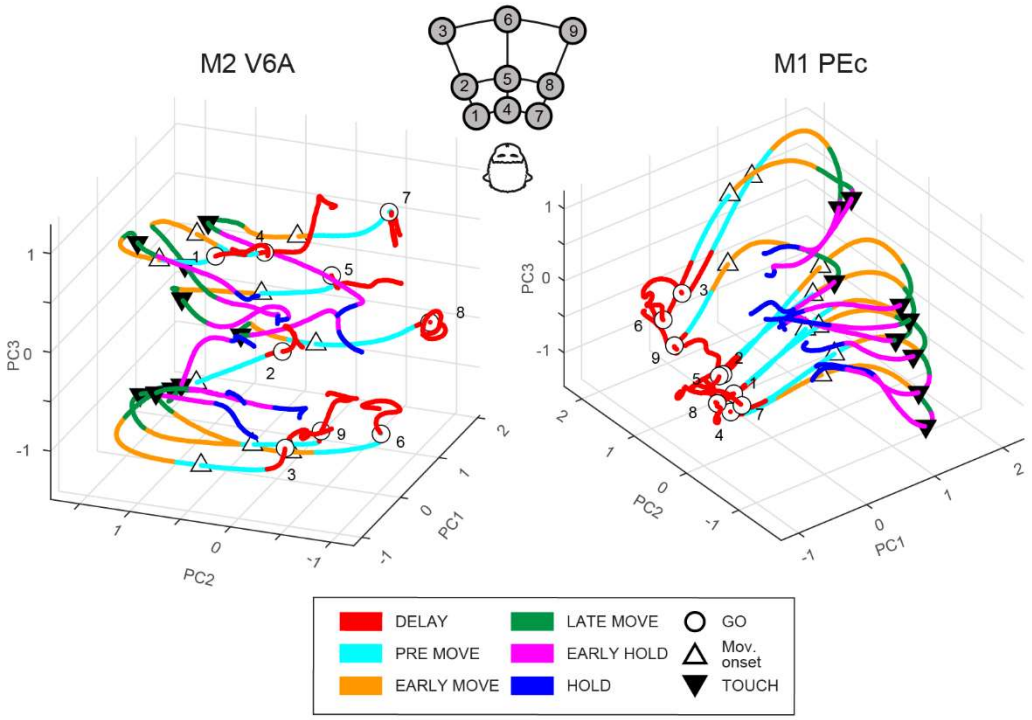

Figure 19. Neural trajectories and HMM-based segmentation for the other 2 neural populations. Same conventions as Figure 18. From Diomedi et al. 2021.

To further confirm quantitatively that each state was associated with a characteristic path of the neural trajectory and to quantify the evolution of neural trajectories, we segmented the trajectories based on the HMM states (Figure 18b). To this end, we calculated the mean pairwise Euclidean distance between points belonging to segments of the same state (intra-state distance) or different states (inter-state distance). The intra-state distance was significantly lower than the inter-state distance for all the 4 (2 animals x 2 areas) neural populations, indicating that segments (and so, population activity dynamics) were more similar within states than between different states (intra-state distance: 0.17 [0.13 0.19] vs inter-state: 0.41 [0.32 0.52], median [25^{th} 75^{th} quantiles]; Wilcoxon test, $p<0.001$). In conclusion, despite the strong assumption on stationarity that is inherent in the HMM method, it still captured the complex neural dynamics of the population activity.

5 Discussion

In the present study we examined the dynamics of the population activity in two medial parietal areas, namely V6A and PEc, well known to contain highly heterogeneous populations that process a variety of spatial and motor features and are active during several phases of the arm reaching task. Using HMMs and PCA analysis we have shown the validity of the first hypothesis made in the introduction: neural states detected are stable across different trials and they are time locked to the behavioural of the animal. Furthermore, we found these neural dynamics to be strikingly similar to those reported in motor and premotor cortices, thus highlighting common computational principles during motor control.

5.1 Time course of 'macro' states supports anatomical and functional parieto-frontal gradients

Along the task progress, we observed three main hidden neural states i.e., DELAY, MOVE and HOLD in the two parietal areas ('macro' states). The transition between the DELAY and MOVE states occurred about 60 ms before the movement onset (45 and 75 ms in V6A and PEc, respectively). This transition could reflect a shift from a visuospatial encoding of target location using eye position signals to a somatomotor processing related to the upcoming arm movement. Strong eye position signals have been indeed reported both in V6A and in PEc (Breveglieri et al., 2012; Diomedi et al., 2020; Galletti et al., 1995; Raffi et al., 2008). Note that HMM did not take into account eye position information and, in addition, the possibility to discriminate these three neural states (DELAY, MOVE, HOLD) cannot be attributed to this factor because the animal continuously fixated the target during the analyzed task interval. On the other hand, neural activity related to gaze position probably differentiated DELAY neural states across different targets.

The MOVE state rose before the movement onset, probably carrying information about an efferent copy of the motor command sent to PPC to construct a forward model of the movement state (Mulliken et al., 2008a). The most likely source of efferent copy signals is the dorsal premotor cortex (PMd) that sends feedback projections to V6A and PEc (Bakola et al., 2010; Gamberini et al., 2009; Johnson et al., 1996). In this regard, a reaching study in PMd (Kermere et al., 2008) using HMMs reported that the MOVE state emerged about 100 ms before movement onset, thus leading by 55 and 25 ms the MOVE state in V6A and PEc, respectively. This timeline, despite differences in tasks with Kermere et al. (2008), is consistent with an anterior-to-posterior propagation of movement-related signals in the parieto-frontal reaching network.

The transition from MOVE to HOLD state was detected about 40 ms (60 and 15 ms, respectively for V6A and PEc) after the end of movement, thus suggesting that HOLD state encoded somatosensory responses that are known to occur 30-50 ms after stimulation (Cameron et al., 2014; Fetz et al., 1980; Fromm and Evarts, 1981; Soso and Fetz 1980). The slightly earlier transition to HOLD in PEc compared to V6A could be attributed to the fact that PEc receives strong somatic inputs directly from PE and area 2 of the somatosensory cortex (Bakola et al., 2010), whereas V6A receives these inputs indirectly from PEc (Gamberini et al., 2009, 2020).

Compared to parietal, in frontal cortex (ventral premotor cortex, PMv) the hold state emerged about 95 ms after the movement end (Mazurek et al., 2018). In sum, the time course of the 'macro' states reported here agrees both with large-scale theory on motor control (Todorov and Jordan, 2002) and with recent views on PPC organization (Andresen et al., 2014; Gamberini et al., 2020; Hadjidimitrakis et al., 2019; Medendorp and Heed 2019).

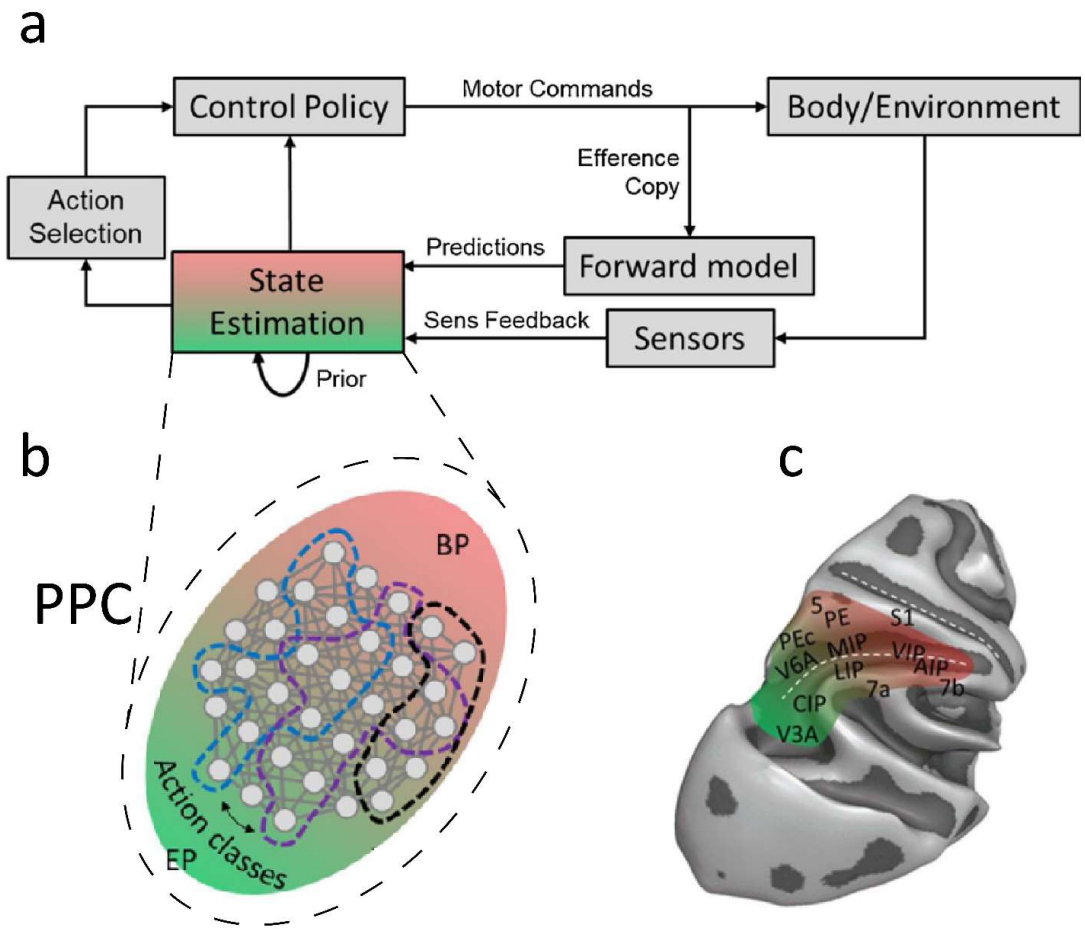

Figure 20 Diagram of the large-scale Optimal Feedback Control and PPC functional gradients. a) Optimal Feedback Control, state estimator combines prediction (elaborated by an internal forward model), sensory feedback and expected sensory state (prior). Action selection process specifies the behavioural goal, control policy specifies how to act. b) Schematic representation of the two gradients of PPC. BP = body-related pole, EP environment-related pole. Colors represent the rostral-to-caudal gradient. c) Overlay between PPC estimator state model and 3D reconstruction of

macaque brain. Dashed line indicates the central sulcus and the interparietal sulcus. Colors represent the rostral-to-caudal gradient. Modified from Medendorp and Heed 2019.

The resulting timing delay, comparing the neural state transitions of motor cortices and PPC, is in agreement with the theory of the Optimal Feedback Control (OFC, Figure 20a) proposed by Todorov and Jordan (2002). The theory explains that during goal directed movement three main processes occur: first the system identification process that allows the prediction of the sensory consequences of a motor command, then the state estimation process combines these predictions with current sensory feedback information (internal forward model) in order to estimate the state of the body in the world. Finally, the optimal control process modifies the gains of the sensorimotor feedback loops to improve the movement performance. In this framework, the role of state estimator is interpreted by the posterior parietal cortex.

Furthermore, the time difference (on average 35 ms) in the states transition between PEc (first) and V6A (second) supports revised views on PPC by Medendorp and Heed (2019). In agreement with this work, the PPC is included within the OFC model as a 'state estimator' and two gradients have here been defined: a rostral-to-caudal gradient that projects the body in relation to the environment and a medial-to-lateral gradient for action classes. The timing difference between PEc and V6A fits well into the framework of the rostral-to-caudal gradient that connects the caudal pole that mainly projects body information to the environment to the rostral one performing the opposite function (Medendorp and Heed 2019). Furthermore, recent accounts based on the anatomical inputs and on the functional properties of V6A allows to consider this area to be associated with a more visual function (visuomotor), conversely area PEc is more somatic (somatomotor) (Gamberini et al., 2020). It could be argued that these two areas lie just in between these poles (Figure 20b-c).

5.2 'Micro' states could reflect several sensorimotor processes

In a data driven fashion, we analyzed restricted trial periods to test whether a finer segmentation of population activity was possible. We did find additional 'micro' states that were detected in a variable percentage of the emission sequences and therefore their average probability remained lower than the 'macro' states. Accordingly, the 'micro' states were associated with more transient and weaker cell activation patterns. First, PREMOVE state extended within the movement reaction time (~70 ms after the 'go' signal until 30 ms before movement start). This suggests that PREMOVE reflected a stimulus-driven activity pattern that triggered an internally determined movement preparation period. The 70-ms interval between the 'go' signal and PREMOVE rise is consistent with visual processing

latencies in PPC (Kutz et al., 2003; Mulliken et al., 2008a). Although PREMOVE likely reflects sensory processing, processing related also to motor preparation cannot be excluded. A combination of both sensory and motor processing delays in the reaction time activity was reported in PMd (Thura and Cisek, 2014). In PMd, Kemere and colleagues (2008) reported a transition to a planning HMM state occurring about 100 ms *after* the 'go' signal, in line with earlier visual processing in parietal compared to premotor cortex (Cisek and Kalaska, 2010).

Similarly to PREMOVE, the EARLY HOLD followed a behavioural event, emerging slightly after the movement end. It was followed by the HOLD state that included the rest of the holding period. EARLY HOLD could reflect phasic somatosensory discharges related to the initial touch of the target and the subsequent hand stabilization transient phase, whereas HOLD could represent tonic activity required for the maintenance of arm posture. Both phasic and tonic signals related to arm posture have been reported in somatosensory cortex and area PE (Georgopoulos et al., 1984; Hamel-Paquet et al., 2006; Soso and Fetz 1980) and they could be relayed to PEc and V6A (Bakola et al., 2010; Gamberini et al., 2020). EARLY HOLD states give also insight about the different nature/functional role of these two areas: the temporal evolution of this state (Figure 13a) in PEc is identical in both animals and on the contrary in V6A is more variable. This could be due to a more sensory role of PEc due to its time-locked activity at the stimulus (in this case touch and proprioceptive).

Another important aspect regards the nature of neural representations during MOVE state. Besides the well-established role in the visuospatial encoding of motor goals (Andersen et al., 2014), parietal cortex is also involved in the arm movement trajectory planning and online control (Archambault et al., 2009; Mulliken et al., 2008b; Torres et al., 2013). From behavioural data, arm movement velocity has been reported to show a roughly bell-shaped profile with peak velocity reached approximately 40-50% after the movement start (Castiello et al., 2019; Churchland et al., 2006; Roy et al., 2000). Consistent with behaviour, our HMM algorithm detected two 'micro' states within the movement period that well corresponded to the acceleration and deceleration phases, respectively, of the arm movement, with their transition occurring half-way through the movement. To our knowledge, a temporal segmentation of population activity like the one observed here has been reported only recently in primary motor cortex where two Markov hidden states coupled to the acceleration and deceleration of the arm were identified (Kadmon Harpaz et al., 2019). Considering that V6A and PEc are caudal PPC areas located far from motor output, this similarity in temporal structure of movement activity is noteworthy. In motor cortex, it was proposed that the two HMM states could originate from the sequential recruitment of two different subpopulations that would drive agonist muscles during acceleration phase and antagonist during deceleration phase (Hoffman and Strick 1990; Kadmon Harpaz et al., 2019).

An alternative view posits that neural computations and their neural states are shaped by behavioural constraints (Jin et al., 2014; Suway et al., 2018). Indeed, since during reaching there are two main behavioural constraints, i.e. movement start (mostly feedforward) and end (feedback) it is plausible to have two separate states of neural activity. Importantly, the fact that these two states were observed in both parietal and motor cortical areas that lie at different levels in the sensorimotor network, strongly supports this alternative view and suggest that it is a general principle. Accordingly, it is likely that parieto-frontal areas do not control movement in a hierarchical manner but show synchronized intrinsic network dynamics to prepare and generate and execute movements. In this view, even if the dynamics in parietal and frontal areas share the same temporal structure, the information they carry could be qualitatively different due to the heterogeneity of the parietal neurons and the variety of their sensory inputs. In this work, due to the simplicity of the motor task used and the static conditions, we have been able to highlight mainly the temporal similarities between the two nodes of the fronto-parietal network. To unravel more structural and information processing differences, further studies are necessary that will involve more complex tasks with sensory perturbations (e.g. target/hand perturbations, interceptive movements) and task context information (e.g. serial movements, anti-reaches).

5.3 Neural states support 'mixed selectivity'

To gain more insight into the underlying mechanisms, we examined the contribution of single neurons in the main HMM states. Gini index analysis revealed that in both parietal areas, the neurons in the population were on average active during two 'macro' states.

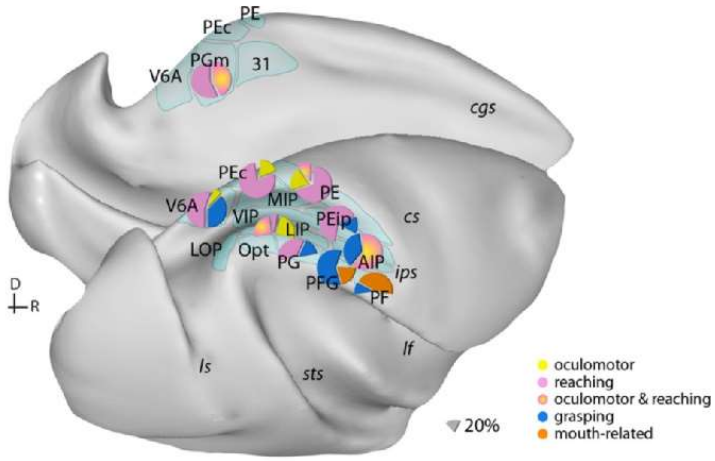

Figure 21 Distribution of different multiple movement signals related to different effectors in PPC. Dorsal and medial view of macaque brain. Data derived from electrophysiological studies: Ferraina et al., 1997 (PGm); Battaglia-Mayer et al., 2001 (PEc); Dickinson et al., 2003 (LIP); Kutz et al., 2003; Fattori et al., 2005, 2010 (V6A); Gardner et al., 2007 (PEip); Rozzi et al., 2008 (PG, PFG, PF); Archambault et al., 2009 (PE). Modified from Hadjidimitrakis et al., 2019.

This clearly demonstrates that the subpopulations that contributing to individual neural states showed an extensive overlap. This finding is in line with a recent view supported by anatomical connections and experimental evidence that parietal neurons encode simultaneously a mixture of spatial and movement representations (Figure 21, Hadjidimitrakis et al., 2019).

This view was further confirmed in V6A (Diomedi et al., 2020). In this work, by developing a metric called 'w-value', the authors calculated for each neuron which are the significant parameters that modulate its activity. In this way they showed that V6A neurons are characterised by 'mixed selectivity', i.e. there are few neurons whose activity is explained by only one parameter whereas the majority of neurons process a set of parameters (Figure 22). So, since parietal neurons encode several parameters, and in each behavioural epochs there are the variation of subset parameters, consequently subpopulations that processed neural states show overlap.

'Mixed selectivity' neurons have been found in other species, such as in the PPC of the rat (Raposo et al., 2014) and a different version called ''partial mixed selectivity'' in human anterior intraparietal area (Zhang et al., 2017). Recently, it has been proved that the mixed selectivity scheme is an optimal way to encode several signals. It allows to achieve high dimensionality in the neural representation and then, using simple linear readout, it can generate several potential responses (Fusi et al., 2016).

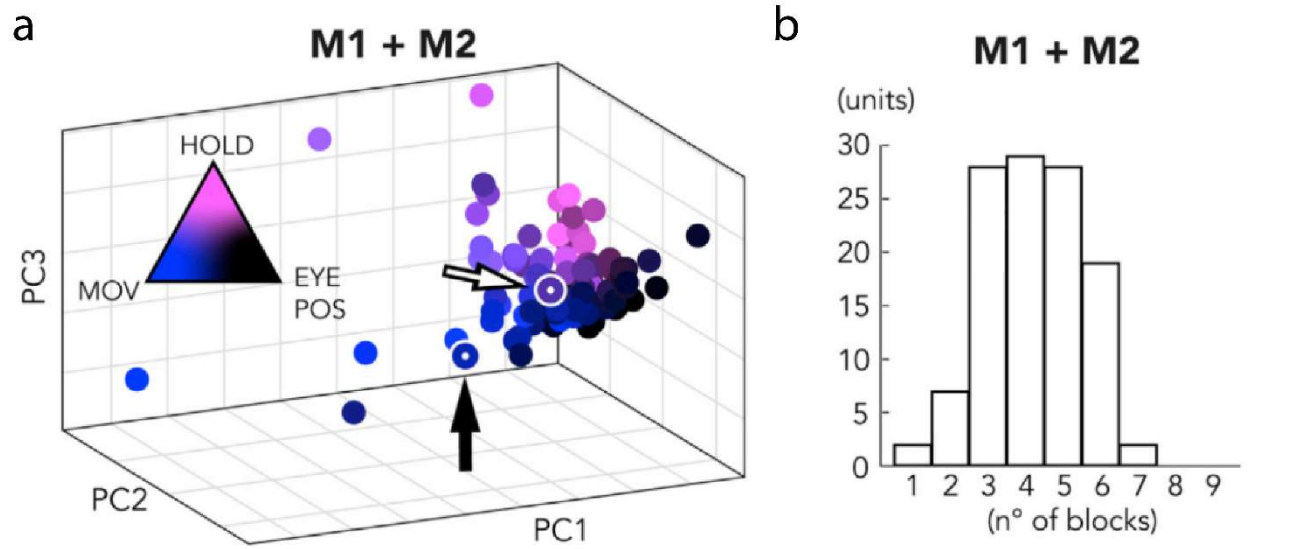

Figure 22 Mixed Selectivity in V6A. a) Principal components analysis of V6A neural population performed on the w-values. Every dot represents a cell. Each point is colored by combining the colors of the main modulating parameters (parameters of the MOVE (MOVE), HOLD (HOLD) epochs and gaze position (EYE POS)) in accordance with their w-values. This shows that there are not clusters inside the population and only few cells maintain pure color. Black arrow indicated selective neuron; white arrow indicated neuron with a mixed modulation. b) Histogram showing the number of parameters needed to explain the 85% of neural activity of each neuron. Modified from Diomedi et al., 2020.

5.4 Single-cell activity modulations and population activity covariance support HMM states

Despite being active during multiple states, single neurons of V6A and PEc showed clear modulations of activity in the transitions between both 'macro' and 'micro' states. To evaluate the effect of these single neural behaviors on the ensemble activity, we adopted a population approach different from HMM and explored the population dynamics in continuous neural space using PCA analyses. In particular, recent evidence from motor and premotor cortex suggests that population activity can be represented in the low-dimensional space by a unique neural trajectory with specific dynamics (Afshar et al., 2011; Churchland et al., 2012; Kadmon Harpaz et al., 2019; Petreska et al., 2011).

Similarly, we found here that parietal ensemble activity was represented by smooth trajectories that reflected the spatio-temporal features of the task. Superimposing the neural trajectory of the population activity in the various task conditions with the neural states, we observed that they were not represented by separated points (or small clouds of points), as it would be expected given that stationary firing rate within a state is assumed for Markov processes, but by segments with characteristic paths (Figure 18 and 19). This result further confirmed the HMMs findings and paves the way for a more detailed exploration of parietal neural dynamics during various tasks with state space methods.

Another interesting finding of the neural trajectories' analysis regarded the relative extent of the various states in the neural space. With respect to the states immediately before (PREMOV), during (MOV) and just after the arm movement (EARLY HOLD), the activity in the initial (DELAY) and final (HOLD) states was much less dynamic. This could be attributed to the fact that our task involved mostly stable sensory processing, with static eye and arm position signals present in DELAY and HOLD states.

5.5 Limitations, future directions and conclusions

Overall, it should be acknowledged that our task was somehow biased towards motor-related processing and neural dynamics in parietal cortex should be also studied under more dynamic sensory stimulation (e.g. target/hand perturbation, interceptive movements, bimanual coordination) to study how feedback loops are integrated in population dynamics. Moreover, since the present study focused only on a restricted part of medial PPC, it remains to be shown whether motor-like neural dynamics are present in other neighbouring areas. In this regard, there is recent evidence that during grasping control the lateral PPC, area AIP exhibits neural dynamics very similar to that of area F5 of the ventral

part of premotor cortex (Michaels et al., 2018). Future work is needed to describe the motor neural dynamics in other associative and cognitive areas of the parietal cortex.

Another limitation of our study is that no recordings of arm kinematics and muscle activity were performed. This information would have helped us to give a better functional characterisation of the microstates, especially those that emerged during movement and hold phase. In particular, EMG and kinematics could help us to understand how the movement phases are related to specific patterns of muscle activities during reaching and during the stabilization of the hand.

An interesting outcome of the analysis here presented could be the application of information carried by parietal neural states on the field of brain Computer Interfaces (BMI). Parietal areas have more recently been considered as source of information useful to feed cortical prosthetics (Andersen et al., 2014, Filippini et al., 2018). A crucial point is the detection of the movement intention and here we have shown that it is possible to decode the movement state in two parietal areas, before the actual movement onset. Furthermore, micro states are additional information that can be used to improve such motor prosthetics. Furthermore, it will be very interesting to use HMM to decode relevant information. Actually, in these neural states two types of information are encoded at the same time: the temporal progression of the task (e.g. DELAY, MOVE) and the target position. Comparing the encoded information in the two areas, we do not expect a difference in the decoding of the temporal information, because, as already seen, macro neural states were stable and time locked to the task events. On the contrary, prompted by the somewhat different contributions of the two areas in visuospatial and somatomotor processing (Gamberini et al., 2020; Hadjidimitrakis et al., 2014, 2015, 2019), we would expect a slightly better accuracy in target decoding from V6A in comparison to PEc.

In conclusion, the present work highlights important similarities between parietal and motor cortices population activity not reported before. These results support the interpretation of the parietal cortex as a dynamic computational node that is able to cancel out extrinsic inputs and tune its population activity with the premotor and motor cortices to generate movement.

6 Bibliography

1. Abeles, M., Bergman, H., Gat, I., Meilijson, I., Seidemann, E., Tishby, N., Vaadia, E. (1995). Cortical activity flips among quasi-stationary states. Proceedings of the National Academy of Sciences, 92(19), 8616–8620.

2. Aflalo, T. N., Graziano, M. S. A. (2006). Possible Origins of the Complex Topographic Organization of Motor Cortex: Reduction of a Multidimensional Space onto a Two-Dimensional Array. Journal of Neuroscience, 26(23), 6288–6297.

3. Afshar, A., Santhanam, G., Yu, B. M., Ryu, S. I., Sahani, M., Shenoy, K. V. (2011). Single-trial neural correlates of arm movement preparation. Neuron, 71(3), 555–564.

4. Andersen, R.A., Snyder, L.H., Bradley, D.C., Xing, J. (1997) Multimodal representation of space in the posterior parietal cortex and ist use in planning movements. Annu Rev Neurosci 20:303–330.

5. Andersen, R. A., Kellis, S., Klaes, C., Aflalo, T. (2014). Toward more versatile and intuitive cortical brain-machine interfaces. Current biology: CB, 24(18), R885–R897.

6. Archambault, P. S., Caminiti, R., Battaglia-Mayer, A. (2009). Cortical mechanisms for online control of hand movement trajectory: the role of the posterior parietal cortex. Cerebral cortex (New York, N.Y.: 1991), 19(12), 2848–2864.

7. Ashe, J., Georgopoulos, A. P. (1994). Movement parameters and neural activity in motor cortex and area 5. Cerebral cortex (New York, N.Y. : 1991), 4(6), 590–600.

8. Bakola, S., Gamberini, M., Passarelli, L., Fattori, P., Galletti, C. (2010). Cortical connections of parietal field PEc in the macaque: linking vision and somatic sensation for the control of limb action. Cerebral cortex (New York, N.Y. : 1991), 20(11), 2592–2604.

9. Bakola, S., Passarelli, L., Gamberini, M., Fattori, P., Galletti, C. (2013). Cortical Connectivity Suggests a Role in Limb Coordination for Macaque Area PE of the Superior Parietal Cortex. Journal of Neuroscience, 33(15), 6648–6658.

10. Bakola, S., Passarelli, L., Huynh, T., Impieri, D., Worthy, K. H., Fattori, P., Galletti, C., Burman, K. J., Rosa, M. G. P. (2017). Cortical Afferents and Myeloarchitecture Distinguish the Medial Intraparietal Area (MIP) from Neighboring Subdivisions of the Macaque Cortex. Eneuro, 4(6), ENEURO.0344-17.2017.

11. Bardella, G., Pani, P., Brunamonti, E., Giarrocco, F., Ferraina, S. (2020). The small scale functional topology of movement control: Hierarchical organization of local activity anticipates movement generation in the premotor cortex of primates. NeuroImage, 207, 116354.

12. Batista, A. P., Buneo, C. A., Snyder, L. H., Andersen, R. A. (1999). Reach plans in eye-centered coordinates. Science (New York, N.Y.), 285(5425), 257–260.

13. Battaglia-Mayer, A., Ferraina, S., Genovesio, A., Marconi, B., Squatrito, S., Molinari, M., Lacquaniti, F., Caminiti, R. (2001). Eye-hand coordination during reaching. II. An analysis of the relationships between visuomanual signals in parietal cortex and parieto-frontal association projections. Cerebral cortex (New York, N.Y. : 1991), 11(6), 528–544.

14. Beevor, C., and Horsley, V. (1890). An experimental investigation into the arrangement of excitable fibres of the internal capsule of the bonnet monkey (Macacus sinicus). Philos. Trans. R. Soc. Lond. B Biol. Sci. 181, 49–88.

15. Bicego, M., Castellani, U., Murino, V. (2005). A Hidden Markov Model approach for appearance-based 3D object recognition. Pattern Recognition Letters, 26(16), 2588–2599.

16. Bollimunta, A., Totten, D., Ditterich, J. (2012). Neural dynamics of choice: single-trial analysis of decision-related activity in parietal cortex. The Journal of neuroscience : the official journal of the Society for Neuroscience, 32(37), 12684–12701.

17. Bosco, A., Breveglieri, R., Chinellato, E., Galletti, C., Fattori, P. (2010). Reaching Activity in the Medial Posterior Parietal Cortex of Monkeys Is Modulated by Visual Feedback. 13.

18. Breveglieri, R., Kutz, D. F., Fattori, P., Gamberini, M., Galletti, C. (2002). Somatosensory cells in the parieto-occipital area V6A of the macaque: NeuroReport, 13(16), 2113–2116.

19. Breveglieri, R., Galletti, C., Gamberini, M., Passarelli, L., Fattori, P. (2006). Somatosensory Cells in Area PEc of Macaque Posterior Parietal Cortex. 6.

20. Breveglieri, R., Galletti, C., Monaco, S., Fattori, P. (2008). Visual, Somatosensory, and Bimodal Activities in the Macaque Parietal Area PEc. Cerebral Cortex, 18(4), 806–816.

21. Breveglieri, R., Hadjidimitrakis, K., Bosco, A., Sabatini, S. P., Galletti, C., Fattori, P. (2012). Eye position encoding in three-dimensional space: integration of version and vergence signals in the medial posterior parietal cortex. The Journal of neuroscience: the official journal of the Society for Neuroscience, 32(1), 159–169.

22. Breveglieri, R., Galletti, C., Dal Bò, G., Hadjidimitrakis, K., Fattori, P. (2014). Multiple Aspects of Neural Activity during Reaching Preparation in the Medial Posterior Parietal Area V6A. Journal of Cognitive Neuroscience, 26(4), 878–895.

23. Breveglieri, R., Galletti, C., Bosco, A., Gamberini, M., Fattori, P. (2015). Object Affordance Modulates Visual Responses in the Macaque Medial Posterior Parietal Cortex. Journal of Cognitive Neuroscience, 27(7), 1447–1455.

24. Cameron, B. D., de la Malla, C., López-Moliner, J. (2014). The role of differential delays in integrating transient visual and proprioceptive information. Frontiers in psychology, 5, 50.

25. Caminiti R, Innocenti GM, Battaglia-Mayer A (2015) Organization and evolution of parieto-frontal processing streams in macaque monkeys and humans. Neurosci Biobehav Rev 56:73–96.

26. Campbell, A.W. (1905). Histological Studies on the Localization of Cerebral Function (Cambridge University Press).

27. Castiello, U., Dadda, M. (2019). A review and consideration on the kinematics of reach-to-grasp movements in macaque monkeys. Journal of neurophysiology, 121(1), 188–204.

28. Churchland, M. M., Santhanam, G., Shenoy, K. V. (2006). Preparatory activity in premotor and motor cortex reflects the speed of the upcoming reach. Journal of neurophysiology, 96(6), 3130–3146.

29. Churchland, M. M., Shenoy, K. V. (2007). Temporal complexity and heterogeneity of single-neuron activity in premotor and motor cortex. Journal of neurophysiology, 97(6), 4235–4257.

30. Churchland, M. M., Cunningham, J. P., Kaufman, M. T., Ryu, S. I., Shenoy, K. V. (2010). Cortical preparatory activity: representation of movement or first cog in a dynamical machine? Neuron, 68(3), 387–400.

31. Churchland, M. M., Cunningham, J. P., Kaufman, M. T., Foster, J. D., Nuyujukian, P., Ryu, S. I., Shenoy, K. V. (2012). Neural population dynamics during reaching. Nature, 487(7405), 51–56.

32. Cisek, P., Kalaska, J. F. (2010). Neural mechanisms for interacting with a world full of action choices. Annual review of neuroscience, 33, 269–298.

33. Cunningham, J. P., Yu, B. M. (2014). Dimensionality reduction for large-scale neural recordings. Nature Neuroscience, 17(11), 1500–1509.

34. Dickinson, A. R., Calton, J. L., and Snyder, L. H. (2003). Nonspatial saccadespecific activation in area LIP of monkey parietal cortex. J. Neurophysiol. 90, 2460–2464.

35. Diomedi, S., Vaccari, F. E., Filippini, M., Fattori, P., Galletti, C. (2020). Mixed Selectivity in Macaque Medial Parietal Cortex during Eye-Hand Reaching. iScience, 23(10), 101616.

36. Diomedi, S., Vaccari, F. E., Galletti, C., Hadjidimitrakis, K., Fattori, P. (2021). Motor-like neural dynamics in two parietal areas during arm reaching. Progress in Neurobiology, 102116.

37. Evarts E. V. (1968). Relation of pyramidal tract activity to force exerted during voluntary movement. Journal of neurophysiology, 31(1), 14–27.

38. Fattori, P., Gamberini, M., Kutz, D. F., Galletti, C. (2001). 'Arm-reaching' neurons in the parietal area V6A of the macaque monkey. The European journal of neuroscience, 13(12), 2309–2313.

39. Fattori, P., Kutz, D. F., Breveglieri, R., Marzocchi, N., Galletti, C. (2005). Spatial tuning of reaching activity in the medial parieto-occipital cortex (area V6A) of macaque monkey. European Journal of Neuroscience, 22(4), 956–972.

40. Fattori, P., Raos, V., Breveglieri, R., Bosco, A., Marzocchi, N., Galletti, C. (2010). The Dorsomedial Pathway Is Not Just for Reaching: Grasping Neurons in the Medial Parieto-Occipital Cortex of the Macaque Monkey. Journal of Neuroscience, 30(1), 342–349.

41. Fattori, P., Breveglieri, R., Bosco, A., Gamberini, M., Galletti, C. (2017). Vision for Prehension in the Medial Parietal Cortex. Cerebral cortex (New York, N.Y. : 1991), 27(2), 1149–1163.

42. Ferraina, S., Garasto, M. R., Battaglia-Mayer, A., Ferraresi, P., Johnson, P. B., Lacquaniti, F., Caminiti, R. (1997). Visual control of hand-reaching movement: activity in parietal area 7m. The European journal of neuroscience, 9(5), 1090–1095.

43. Ferraina, S., Battaglia-Mayer, A., Genovesio, A., Marconi, B., Onorati, P., Caminiti, R. (2001) Early coding of visuomanual coordination during reaching in parietal area PEc. J Neurophysiol 85:462–467.

44. Fetz, E. E., Finocchio, D. V., Baker, M. A., Soso, M. J. (1980). Sensory and motor responses of precentral cortex cells during comparable passive and active joint movements. Journal of neurophysiology, 43(4), 1070–1089.

45. Fetz, E. E. (1992). Are movement parameters recognizably coded in the activity of single neurons? In P. Cordo & S. Harnad (A c. Di), Movement Control (1ª ed., pagg. 77–88). Cambridge University Press.

46. Filimon, F. (2010). Human cortical control of hand movements: parietofrontal networks for reaching, grasping, and pointing. Neurosci 16:388–407.

47. Filippini, M., Breveglieri, R., Hadjidimitrakis, K., Bosco, A., Fattori, P. (2018). Prediction of Reach Goals in Depth and Direction from the Parietal Cortex. Cell Reports, 23(3), 725–732.

48. Finkelstein, A., Ulanovsky, N., Tsodyks, M., Aljadeff, J. (2018). Optimal dynamic coding by mixed-dimensionality neurons in the head-direction system of bats. Nature communications, 9(1), 3590.

49. Fromm, C., Evarts, E. V. (1981). Relation of size and activity of motor cortex pyramidal tract neurons during skilled movements in the monkey. The Journal of neuroscience : the official journal of the Society for Neuroscience, 1(5), 453–460.

50. Fulton, J. (1934). Forced grasping and groping in relation to the syndrome of the premotor area. Arch. Neurol. Psychiatry 31, 221–235.

51. Fulton, J. (1935). A note on the definition of the ‘‘motor’’ and ‘‘premotor’’ areas. Brain 58, 311–316.

52. Fusi, S., Miller, E. K., Rigotti, M. (2016). Why neurons mix: High dimensionality for higher cognition. Current Opinion in Neurobiology, 37, 66–74.

53. Gallego, J. A., Perich, M. G., Miller, L. E., Solla, S. A. (2017). Neural Manifolds for the Control of Movement. Neuron, 94(5), 978–984.

54. Gallego, J. A., Perich, M. G., Naufel, S. N., Ethier, C., Solla, S. A., Miller, L. E. (2018). Cortical population activity within a preserved neural manifold underlies multiple motor behaviors. Nature communications, 9(1), 4233.

55. Galletti, C., Battaglini, P. P., Fattori, P. (1995). Eye position influence on the parieto-occipital area PO (V6) of the macaque monkey. The European journal of neuroscience, 7(12), 2486–2501.

56. Galletti, C., Fattori, P., Battaglini, P. P., Shipp, S., Zeki, S. (1996). Functional Demarcation of a Border Between Areas V6 and V6A in the Superior Parietal Gyrus of the Macaque Monkey. European Journal of Neuroscience, 8(1), 30–52.

57. Galletti, C., Fattori, P., Kutz, D. F., Gamberini, M. (1999). Brain location and visual topography of cortical area V6A in the macaque monkey. The European journal of neuroscience, 11(2), 575–582.

58. Galletti, C., Gamberini, M., Kutz, D. F., Fattori, P., Luppino, G., Matelli, M. (2001). The cortical connections of area V6: An occipito-parietal network processing visual information: Cortical connections of area V6. European Journal of Neuroscience, 13(8), 1572–1588.

59. Galletti, C., Fattori, P. (2003). Neuronal mechanisms for detection of motion in the field of view. Neuropsychologia, 41(13), 1717–1727.

60. Galletti, C., Kutz, D. F., Gamberini, M., Breveglieri, R., Fattori, P. (2003). Role of the medial parieto-occipital cortex in the control of reaching and grasping movements. Experimental Brain Research, 153(2), 158–170.

61. Galletti, C., Fattori, P., Gamberini, M., Kutz, D. (2004). The Most Direct Visual Pathway to the Frontal Cortex. Cortex, 40(1), 216–217.

62. Galletti, C., Breveglieri, R., Lappe, M., Bosco, A., Ciavarro, M., Fattori, P. (2010). Covert Shift of Attention Modulates the Ongoing Neural Activity in a Reaching Area of the Macaque Dorsomedial Visual Stream. PLoS ONE, 5(11), e15078.

63. Galletti, C., Fattori, P. (2018). The dorsal visual stream revisited: Stable circuits or dynamic pathways? Cortex, 98, 203–217.

64. Gamberini, M., Passarelli, L., Fattori, P., Zucchelli, M., Bakola, S., Luppino, G., Galletti, C. (2009). Cortical connections of the visuomotor parietooccipital area V6Ad of the macaque monkey. The Journal of comparative neurology, 513(6), 622–642.

65. Gamberini, M., Galletti, C., Bosco, A., Breveglieri, R., Fattori, P. (2011). Is the medial posterior parietal area V6A a single functional area?. The Journal of neuroscience : the official journal of the Society for Neuroscience, 31(13), 5145–5157.

66. Gamberini, M., Dal Bò, G., Breveglieri, R., Briganti, S., Passarelli, L., Fattori, P., Galletti, C. (2018). Sensory properties of the caudal aspect of the macaque's superior parietal lobule. Brain structure & function, 223(4), 1863–1879.

67. Gamberini, M., Passarelli, L., Fattori, P., Galletti, C. (2020). Structural connectivity and functional properties of the macaque superior parietal lobule. Brain structure & function, 225(4), 1349–1367.

68. Gamberini, M., Passarelli, L., Impieri, D., Montanari, G., Diomedi, S., Worthy, K. H., Burman, K. J., Reser, D. H., Fattori, P., Galletti, C., Bakola, S., Rosa, M. G. P. (2021). Claustral Input to the Macaque Medial Posterior Parietal Cortex (Superior Parietal Lobule and Adjacent Areas). Cerebral Cortex, bhab108.

69. Gao, P., Ganguli, S. (2015). On simplicity and complexity in the brave new world of large-scale neuroscience. Current opinion in neurobiology, 32, 148–155.

70. Gardner, E. P., Babu, K. S., Reitzen, S. D., Ghosh, S., Brown, A. S., Chen, J., Hall, A. L., Herzlinger, M. D., Kohlenstein, J. B., Ro, J. Y. (2007). Neurophysiology of prehension. I. Posterior parietal cortex and object-oriented hand behaviors. Journal of neurophysiology, 97(1), 387–406.

71. Georgopoulos, A. P., Kalaska, J. F., Caminiti, R., Massey, J. T. (1982). On the relations between the direction of two-dimensional arm movements and cell discharge in primate motor cortex. The Journal of neuroscience : the official journal of the Society for Neuroscience, 2(11), 1527–1537.

72. Georgopoulos, A. P., Caminiti, R., Kalaska, J. F. (1984). Static spatial effects in motor cortex and area 5: quantitative relations in a two-dimensional space. Experimental brain research, 54(3), 446–454.

73. Gottlieb, J. (2007). From thought to action: the parietal cortex as a bridge between perception, action, and cognition. Neuron 53:9–16.

74. Graziano, M. S. A., Aflalo, T. N. (2007). Mapping Behavioral Repertoire onto the Cortex. Neuron, 56(2), 239–251.

75. Graziano M.S. (2008). The Intelligent Movement Machine: An Ethological Perspective on the Primate Motor System,Vol. 224. Oxford/New York: Oxford Univ. Press

76. Graziano M. S. (2011). Cables vs. networks: old and new views on the function of motor cortex. The Journal of physiology, 589(Pt 10), 2439.

77. Grunbaum, A., Sherrington, C. (1903). Observations on the physiology of the cerebral cortex of the anthropoid apes. Proceedings of the Royal Society of London 72, 152–155.

78. Hadjidimitrakis, K., Breveglieri, R., Placenti, G., Bosco, A., Sabatini, S. P., Fattori, P. (2011). Fix Your Eyes in the Space You Could Reach: Neurons in the Macaque Medial Parietal Cortex Prefer Gaze Positions in Peripersonal Space. PLoS ONE, 6(8), e23335.

79. Hadjidimitrakis, K., Breveglieri, R., Bosco, A., Fattori, P. (2012). Three-dimensional eye position signals shape both peripersonal space and arm movement activity in the medial posterior parietal cortex. Frontiers in Integrative Neuroscience, 6. h

80. Hadjidimitrakis, K., Bertozzi, F., Breveglieri, R., Bosco, A., Galletti, C., Fattori, P. (2014). Common neural substrate for processing depth and direction signals for reaching in the monkey medial posterior parietal cortex. Cerebral cortex (New York, N.Y. : 1991), 24(6), 1645–1657.

81. Hadjidimitrakis, K., Dal Bo', G., Breveglieri, R., Galletti, C., Fattori, P. (2015). Overlapping representations for reach depth and direction in caudal superior parietal lobule of macaques. Journal of neurophysiology, 114(4), 2340–2352.

82. Hadjidimitrakis, K., Bertozzi, F., Breveglieri, R., Galletti, C., Fattori, P. (2017). Temporal stability of reference frames in monkey area V6A during a reaching task in 3D space. Brain structure & function, 222(4), 1959–1970.

83. Hadjidimitrakis, K., Bakola, S., Wong, Y. T., Hagan, M. A. (2019). Mixed Spatial and Movement Representations in the Primate Posterior Parietal Cortex. Frontiers in neural circuits, 13, 15.

84. Hadjidimitrakis, K., Ghodrati, M., Breveglieri, R., Rosa, M., & Fattori, P. (2020). Neural coding of action in three dimensions: Task- and time-invariant reference frames for visuospatial and motor-related activity in parietal area V6A. The Journal of comparative neurology, 528(17), 3108–3122.

85. Hamel-Pâquet, C., Sergio, L. E., Kalaska, J. F. (2006). Parietal area 5 activity does not reflect the differential time-course of motor output kinetics during arm-reaching and isometric-force tasks. Journal of neurophysiology, 95(6), 3353–3370.

86. Hatsopoulos, N. G. (2005). Encoding in the Motor Cortex: Was Evarts Right After All? Focus on “Motor Cortex Neural Correlates of Output Kinematics and Kinetics During Isometric-Force and Arm-Reaching Tasks”. Journal of Neurophysiology, 94(4), 2261–2262.

87. Hoffman, D. S., Strick, P. L. (1990). Step-tracking movements of the wrist in humans. II. EMG analysis. The Journal of neuroscience: the official journal of the Society for Neuroscience, 10(1), 142–152.

88. Hwang, E. J., Hauschild, M., Wilke, M., Andersen, R. A. (2014). Spatial and temporal eye-hand coordination relies on the parietal reach region. The Journal of neuroscience: the official journal of the Society for Neuroscience, 34(38), 12884–12892.

89. Hyvärinen, J. (1982). Posterior parietal lobe of the primate brain. Physiological reviews, 62(3), 1060–1129.

90. Jin, X., Tecuapetla, F., Costa, R. M. (2014). Basal ganglia subcircuits distinctively encode the parsing and concatenation of action sequences. Nature neuroscience, 17(3), 423–430.

91. Johnson, P. B., Ferraina, S., Bianchi, L., Caminiti, R. (1996). Cortical networks for visual reaching: physiological and anatomical organization of frontal and parietal lobe arm regions. Cerebral cortex (New York, N.Y. : 1991), 6(2), 102–119.

92 Kadmon Harpaz, N., Ungarish, D., Hatsopoulos, N. G., Flash, T. (2019). Movement Decomposition in the Primary Motor Cortex. Cerebral cortex (New York, N.Y. : 1991), 29(4), 1619–1633.

93. Kalaska, J.F. (1996) Parietal cortex area 5 and visuomotor behavior. Can J Physiol Pharmacol 74:483–498.

94. Kandel, E., Schwartz, J., Jessel, T., Siegelbaum, S., Hudspeth, A.J. (2013) Principles of Neural Science, Fifth Edition.

95. Kang, X., Sarma, S. V., Santaniello, S., Schieber, M., Thakor, N. V. (2015). Task-Independent Cognitive State Transition Detection From Cortical Neurons During 3-D Reach-to-Grasp Movements. IEEE Transactions on Neural Systems and Rehabilitation Engineering, 23(4), 676–682.

96. Kao, J. C., Nuyujukian, P., Ryu, S. I., Shenoy, K. V. (2017). A High-Performance Neural Prosthesis Incorporating Discrete State Selection With Hidden Markov Models. IEEE Transactions on Biomedical Engineering, 64(4), 935–945.

97. Kaufman, M. T., Churchland, M. M., Ryu, S. I., Shenoy, K. V. (2014). Cortical activity in the null space: Permitting preparation without movement. Nature Neuroscience, 17(3), 440–448.

98. Kemere, C., Santhanam, G., Yu, B. M., Afshar, A., Ryu, S. I., Meng, T. H., Shenoy, K. V. (2008). Detecting neural-state transitions using hidden Markov models for motor cortical prostheses. Journal of neurophysiology, 100(4), 2441–2452.

99. Kutz, D. F., Fattori, P., Gamberini, M., Breveglieri, R., Galletti, C. (2003). Early- and late-responding cells to saccadic eye movements in the cortical area V6A of macaque monkey. Experimental brain research, 149(1), 83–95.

100. Kutz, D. F., Marzocchi, N., Fattori, P., Cavalcanti, S., Galletti, C. (2005). Real-time supervisor system based on trinary logic to control experiments with behaving animals and humans. Journal of neurophysiology, 93(6), 3674–3686.

101. Luczak, A., McNaughton, B. L., Harris, K. D. (2015). Packet-based communication in the cortex. Nature reviews. Neuroscience, 16(12), 745–755.

102. Luppino, G., Ben Hamed, S., Gamberini, M., Matelli, M., Galletti, C. (2005). Occipital (V6) and parietal (V6A) areas in the anterior wall of the parieto-occipital sulcus of the macaque: a cytoarchitectonic study. The European journal of neuroscience, 21(11), 3056–3076.

103. Maboudi, K., Ackermann, E., de Jong, L. W., Pfeiffer, B. E., Foster, D., Diba, K., Kemere, C. (2018). Uncovering temporal structure in hippocampal output patterns. eLife, 7, e34467.

104. Matelli, M., Govoni, P., Galletti, C., Kutz, D. F., Luppino, G. (1998). Superior area 6 afferents from the superior parietal lobule in the macaque monkey. The Journal of comparative neurology, 402(3), 327–352.

105. Mazurek, K. A., Rouse, A. G., Schieber, M. H. (2018). Mirror Neuron Populations Represent Sequences of Behavioral Epochs During Both Execution and Observation. The Journal of neuroscience : the official journal of the Society for Neuroscience, 38(18), 4441–4455.

106. Mazurek, K. A., Schieber, M. H. (2019). Mirror neurons precede non-mirror neurons during action execution. Journal of neurophysiology, 122(6), 2630–2635.

107. McGuire, L. M., Sabes, P. N. (2011). Heterogeneous representations in the superior parietal lobule are common across reaches to visual and proprioceptive targets. The Journal of neuroscience : the official journal of the Society for Neuroscience, 31(18), 6661–6673.

108. Medendorp, W. P., Heed, T. (2019). State estimation in posterior parietal cortex: Distinct poles of environmental and bodily states. Progress in neurobiology, 183, 101691.

109. Michaels, J. A., Dann, B., Intveld, R. W., Scherberger, H. (2018). Neural Dynamics of Variable Grasp-Movement Preparation in the Macaque Frontoparietal Network. The Journal of neuroscience : the official journal of the Society for Neuroscience, 38(25), 5759–5773.

110. Mountcastle, V. B., Lynch, J. C., Georgopoulos, A., Sakata, H., Acuna, C. (1975). Posterior parietal association cortex of the monkey: command functions for operations within extrapersonal space. Journal of neurophysiology, 38(4), 871–908.

111. Mulliken, G. H., Musallam, S., Andersen, R. A. (2008a). Forward estimation of movement state in posterior parietal cortex. Proceedings of the National Academy of Sciences of the United States of America, 105(24), 8170–8177.

112. Mulliken, G. H., Musallam, S., Andersen, R. A. (2008b). Decoding trajectories from posterior parietal cortex ensembles. The Journal of neuroscience : the official journal of the Society for Neuroscience, 28(48), 12913–12926.

113. Mussa-Ivaldi, F.A. (1988). Do neurons in the motor cortex encode movement direction? An alternative hypothesis. Neurosci. Lett. 91:106–11.

114. Omrani, M., Kaufman, M. T., Hatsopoulos, N. G., Cheney, P. D. (2017). Perspectives on classical controversies about the motor cortex. Journal of neurophysiology, 118(3), 1828–1848.

115. Pandya, D. N., Seltzer, B. (1982). Intrinsic connections and architectonics of posterior parietal cortex in the rhesus monkey. The Journal of comparative neurology, 204(2), 196–210.

116. Passarelli, L., Rosa, M. G. P., Gamberini, M., Bakola, S., Burman, K. J., Fattori, P., Galletti, C. (2011). Cortical Connections of Area V6Av in the Macaque: A Visual-Input Node to the Eye/Hand Coordination System. Journal of Neuroscience, 31(5), 1790–1801.

117. Passarelli, L., Rosa, M. G. P., Bakola, S., Gamberini, M., Worthy, K. H., Fattori, P., Galletti, C. (2018). Uniformity and Diversity of Cortical Projections to Precuneate Areas in the Macaque Monkey: What Defines Area PGm? Cerebral Cortex, 28(5), 1700–1717.

118. Passarelli, L., Gamberini, M., Fattori, P. (2021). The superior parietal lobule of primates: A sensory-motor hub for interaction with the environment. Journal of Integrative Neuroscience, 20(1), 157.

119. Petreska, B., Yu, B. M., Cunningham, J. P., Santhanam, G., Ryu, S. I., Shenoy, K. V., Sahani, M. (2011). Dynamical segmentation of single trials from population neural data. Adv. Neural Inf. Process. Syst. 24, 756–764 (2011).

120. Pezzulo, G., Cisek, P. (2016). Navigating the Affordance Landscape: Feedback Control as a Process Model of Behavior and Cognition. Trends in Cognitive Sciences, 20(6), 414–424.

121. Pisella, L., Rossetti, Y., Rode, G. (2017). Optic ataxia in Bálint-Holmes syndrome. Ann Phys Rehabil Med 60:148–154.

122. Piserchia, V., Breveglieri, R., Hadjidimitrakis, K., Bertozzi, F., Galletti, C., Fattori, P. (2017). Mixed Body/Hand Reference Frame for Reaching in 3D Space in Macaque Parietal Area PEc. Cerebral Cortex, bhw039.

123. Pitzalis, S., Fattori, P., Galletti, C. (2013). The functional role of the medial motion area V6. Frontiers in Behavioral Neuroscience, 6.

124. Rabiner, L. R. (1989). A tutorial on hidden Markov models and selected applications in speech recognition. Proc. IEEE **77**, 257–286.

125. Raffi, M., Ballabeni, A., Maioli, M. G., Squatrito, S. (2008). Neuronal responses in macaque area PEc to saccades and eye position. Neuroscience, 156(3), 413–424.

126. Raposo, D., Kaufman, M., and Churchland, A. (2014). A category-free neural population supports evolving demands during decisionmaking. Nat. Neurosci. 17, 1784–1792.

127. Reimer, J., Hatsopoulos, N.G. (2009). The problem of parametric neural coding in the motor system. Adv. Exp. Med. Biol. 629:243–59.

128. Rentzeperis, I., Nikolaev, A. R., Kiper, D. C., van Leeuwen, C. (2014). Distributed processing of color and form in the visual cortex. Frontiers in psychology, 5, 932.

129. Rigotti, M., Barak, O., Warden, M. R., Wang, X. J., Daw, N. D., Miller, E. K., Fusi, S. (2013). The importance of mixed selectivity in complex cognitive tasks. Nature, 497(7451), 585–590.

130. Rizzolatti, G., Matelli, M. (2003). Two different streams form the dorsal visual system: Anatomy and functions. Experimental Brain Research, 153(2), 146–157.

131. Roy, A. C., Paulignan, Y., Farnè, A., Jouffrais, C., Boussaoud, D. (2000). Hand kinematics during reaching and grasping in the macaque monkey. Behavioural brain research, 117(1-2), 75–82.

132. Rozzi, S., Ferrari, P. F., Bonini, L., Rizzolatti, G., Fogassi, L. (2008). Functional organization of inferior parietal lobule convexity in the macaque monkey: electrophysiological characterization of motor, sensory and mirror responses and their correlation with cytoarchitectonic areas. The European journal of neuroscience, 28(8), 1569–1588.

133. Sadtler, P. T., Quick, K. M., Golub, M. D., Chase, S. M., Ryu, S. I., Tyler-Kabara, E. C., Yu, B. M., Batista, A. P. (2014). Neural constraints on learning. Nature, 512(7515), 423–426.

134. Santandrea, E., Breveglieri, R., Bosco, A., Galletti, C., Fattori, P. (2018). Preparatory activity for purposeful arm movements in the dorsomedial parietal area V6A: Beyond the online guidance of movement. Scientific Reports, 8(1), 6926.

135. Scott, S. H., Kalaska, J. F. (1995). Changes in motor cortex activity during reaching movements with similar hand paths but different arm postures. Journal of neurophysiology, 73(6), 2563–2567.

136. Scott, S. H., Kalaska, J. F. (1997). Reaching movements with similar hand paths but different arm orientations. I. Activity of individual cells in motor cortex. Journal of neurophysiology, 77(2), 826–852.

137. Scott S. H. (2000). Population vectors and motor cortex: neural coding or epiphenomenon?. Nature neuroscience, 3(4), 307–308.

138. Scott S. H. (2008). Inconvenient truths about neural processing in primary motor cortex. The Journal of physiology, 586(5), 1217–1224.

139. Sereno, M. I., Huang, R. S. (2014). Multisensory maps in parietal cortex. Current opinion in neurobiology, 24(1), 39–46.

140. Shenoy, K. V., Meeker, D., Cao, S., Kureshi, S. A., Pesaran, B., Buneo, C. A., Batista, A. P., Mitra, P. P., Burdick, J. W., Andersen, R. A. (2003). Neural prosthetic control signals from plan activity: NeuroReport, 14(4), 591–596.

141. Shenoy, K. V., Sahani, M., Churchland, M. M. (2013). Cortical Control of Arm Movements: A Dynamical Systems Perspective. Annual Review of Neuroscience, 36(1), 337–359.

142. Shinde, P. P., Shah, S. (2018). A Review of Machine Learning and Deep Learning Applications. 2018 Fourth International Conference on Computing Communication Control and Automation (ICCUBEA), 1–6.

143. Shipp, S., Blanton, M., Zeki, S. (1998). A visuo-somatomotor pathway through superior parietal cortex in the macaque monkey: Cortical connections of areas V6 and V6A: A visuo-somatomotor pathway in the macaque. European Journal of Neuroscience, 10(10), 3171–3193.

144. Soso, M. J., Fetz, E. E. (1980). Responses of identified cells in postcentral cortex of awake monkeys during comparable active and passive joint movements. Journal of Neurophysiology, 43(4), 1090–1110.

145. Squatrito, S., Raffi, M., Maioli, M. G., Battaglia-Mayer, A. (2001). Visual Motion Responses of Neurons in the Caudal Area PE of Macaque Monkeys. The Journal of Neuroscience, 21(4), RC130–RC130.

146. Suway, S. B., Orellana, J., McMorland, A. J. C., Fraser, G. W., Liu, Z., Velliste, M., Chase, S. M., Kass, R. E., Schwartz, A. B. (2018). Temporally Segmented Directionality in the Motor Cortex. Cerebral Cortex, 28(7), 2326–2339.

147. Thura, D., & Cisek, P. (2014). Deliberation and commitment in the premotor and primary motor cortex during dynamic decision making. Neuron, 81(6), 1401–1416.

148. Todorov E. (2000). Direct cortical control of muscle activation in voluntary arm movements: a model. Nature neuroscience, 3(4), 391–398.

149. Todorov, E., Jordan, M. I. (2002). Optimal feedback control as a theory of motor coordination. Nature Neuroscience, 5(11), 1226–1235.

150. Tootell, R. B., Reppas, J. B., Dale, A. M., Look, R. B., Sereno, M. I., Malach, R., Brady, T. J., Rosen, B. R. (1995). Visual motion aftereffect in human cortical area MT revealed by functional magnetic resonance imaging. Nature, 375(6527), 139–141.

151. Torres, E. B., Quian Quiroga, R., Cui, H., Buneo, C. A. (2013). Neural correlates of learning and trajectory planning in the posterior parietal cortex. Frontiers in Integrative Neuroscience, 7.

152. Ungerleider, L.G., Mishkin, M. (1982). Two cortical visual systems. In D.J. Ingle, M.A. Goodale and R.J.W. Mansfield (Eds.), Analysis of Visual Behaviour. Cambridge: MIT Press, 1982, Ch. 18.

153. Vogt, C., and Vogt, O. (1919). Ergebnisse unserer Hirnforschung. Jounrnal Fur Psychologie und Neurologie 25, 277–462.

154. Walker, K. M., Bizley, J. K., King, A. J., Schnupp, J. W. (2011). Multiplexed and robust representations of sound features in auditory cortex. The Journal of neuroscience : the official journal of the Society for Neuroscience, 31(41), 14565–14576.

155. Williams, A. H., Kim, T. H., Wang, F., Vyas, S., Ryu, S. I., Shenoy, K. V., Schnitzer, M., Kolda, T. G., Ganguli, S. (2018). Unsupervised Discovery of Demixed, Low-Dimensional Neural Dynamics across Multiple Timescales through Tensor Component Analysis. Neuron, 98(6), 1099-1115.e8.

156. Yoon, B.J. (2009). Hidden Markov Models and their Applications in Biological Sequence Analysis. Current Genomics, 10(6), 402–415.

157. Zhang, C. Y., Aflalo, T., Revechkis, B., Rosario, E. R., Ouellette, D., Pouratian, N., Andersen, R. A. (2017). Partially Mixed Selectivity in Human Posterior Parietal Association Cortex. Neuron, 95(3), 697-708.e4.